Time-Of-Flight monitoring reveals higher sediment redistribution rates related to burrowing animals than previously assumed

Paulina Grigusova[1], Annegret Larsen[2], Sebastian Achilles[1], Roland Brandl[3], Camilo del Río[4,5], Nina Farwig[6], Diana Kraus[6], Leandro Paulino[7], Patricio Pliscoff[4,8,9], Kirstin Übernickel[10], Jörg Bendix[1]

[1] Laboratory for Climatology and Remote Sensing, Department of Geography, University of Marburg, 35037 Marburg, Germany; paulina.grigusova@staff.uni-marburg.de (P.G.); bendix@geo.uni-marburg.de (J.B.)

[2] Soil Geography and Landscape, Department of Environmental Sciences, Wageningen University & Research, 6700 AA Wageningen, The Netherlands; annegret.larsen@wur.nl

[3] Animal Ecology, Department of Biology, University of Marburg, 35032 Marburg, Germany; brandlr@biologie.uni-marburg.de

[4] Facultad de Historia, Geografía y Ciencia Política, Instituto de Geografía, Pontificia Universidad Católica de Chile, 782-0436 Santiago, Chile; pliscoff@uc.cl; cdelriol@uc.cl

[5] Centro UC Desierto de Atacama, Pontificia Universidad Católica de Chile, 782-0436 Santiago, Chile; cdelriol@uc.cl

[6] Conservation Ecology, Department of Biology, University of Marburg, 35047 Marburg, Germany; diana.kraus@biologie.uni-marburg.de (D.K.); nina.farwig@biologie.uni-marburg.de (N.F.)

[7] Facultad de Agronomía, Universidad de Concepción, 3780000 Chillán, Chile; lpaulino@udec.cl

[8] Facultad de Ciencias Biológicas, Departamento de Ecología, Pontificia Universidad Católica de Chile, 8331150 Santiago, Chile; pliscoff@uc.cl

[9] Center of Applied Ecology and Sustainability (CAPES), Pontificia Universidad Católica de Chile, 8331150 Santiago, Chile; pliscoff@uc.cl

[10] Earth System Dynamics, Department of Geosciences, University of Tübingen, 72076 Tübingen, Germany; kirstin.uebernickel@uni-tuebingen.de

Corresponding author:
Paulina Grigusova
paulina.grigusova@staff.uni-marburg.de

Abstract

Burrowing animals influence surface microtopography and hillslope sediment redistribution, but changes often remain undetected due to a lack of automated high resolution field monitoring techniques. In this study, we present a new approach to quantify microtopographic variations and surface changes caused by burrowing animals and rainfall-driven erosional processes applied to remote field plots in arid and mediterranean Chile. We compared the mass balance of redistributed sediment between burrow and burrow embedding area, quantified the cumulative sediment redistribution caused by animals and rainfall, and upscaled the results to a hillslope scale. The newly developed instrument, a Time-of-Flight camera, showed a very good detection accuracy. The animal-caused cumulative sediment redistribution was 14.6 $cm^3\ cm^{-2}\ year^{-1}$ in the Mediterranean and 16.4 $cm^3\ cm^{-2}\ year^{-1}$ in the arid climate zone. The rainfall-caused cumulative sediment redistribution within areas affected by burrowing animals was higher (-10.4 $cm^3\ cm^{-2}\ year^{-1}$) in the Mediterranean than the arid climate zone (-1.4 $cm^3\ cm^{-2}\ year^{-1}$). Daily sediment redistribution during rainfall within burrows were up to 350% / 40% higher in the mediterranean / arid zone compared to burrow embedding area, and much higher than previously reported in studies not based on continuous microtopographic monitoring. Furthermore, 38% of the sediment eroding from the burrows accumulated within the burrow entrance while 62% was incorporated into overall hillslope sediment flux. The animals burrowed between on average 1.2 – 2.3 times a month and the burrowing intensity increased after rainfall. Our findings can be implemented into long-term soil erosion models that rely on soil processes but do not yet include animal-induced surface processes on microtopographical scales in their algorithms.

Keywords: Biogeomorphology, bioturbation, sediment transport, burrowing animals, rainfall, Time-of-Flight camera, Chile

81

82 **Graphical abstract**

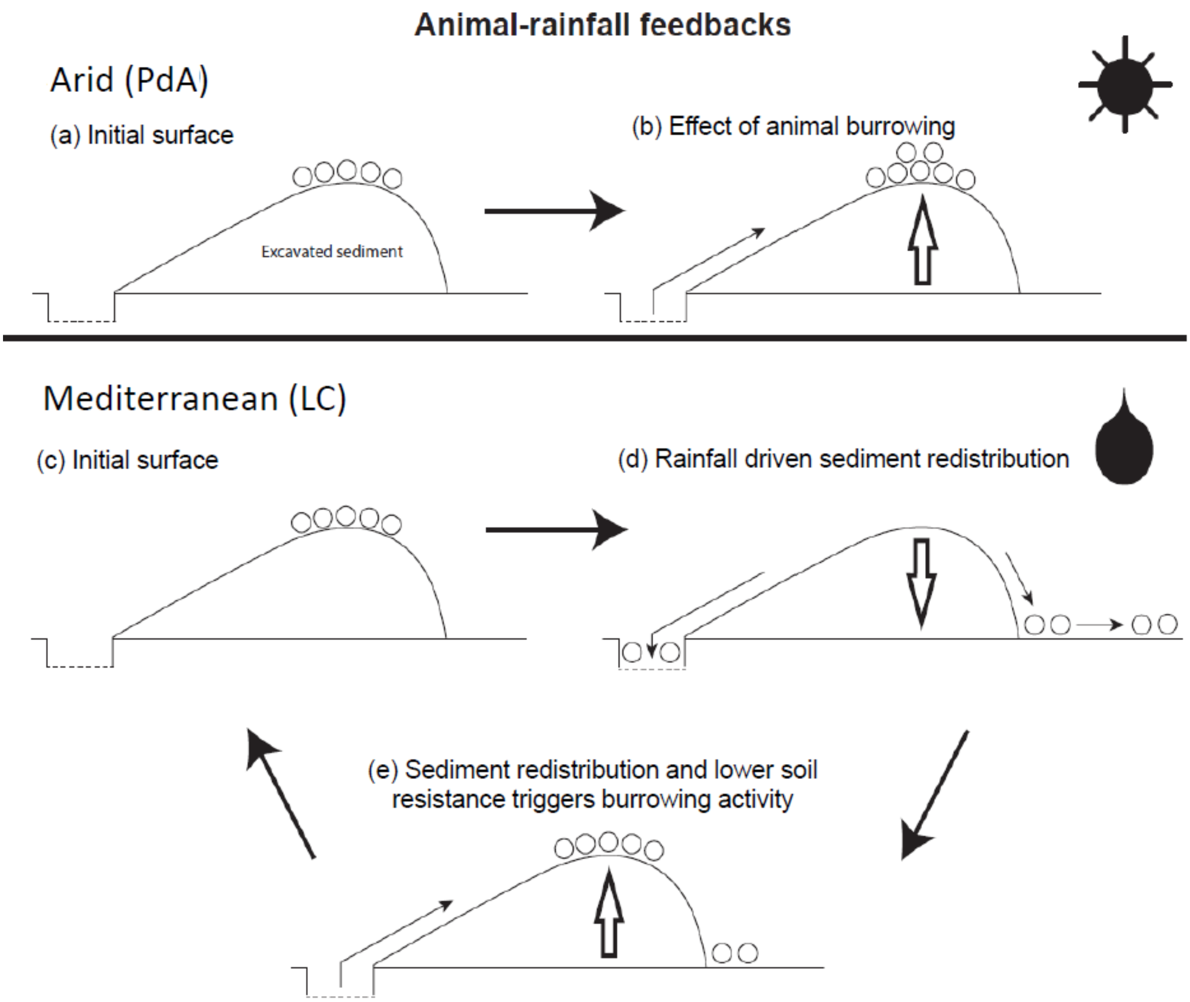

83

84

1. Introduction

Animal burrowing activity affects surface microtopography (Reichman und Seabloom 2002; Kinlaw und Grasmueck 2012), surface roughness (Yair 1995; Jones et al. 2010; Hancock und Lowry 2021) and soil physical properties (Ridd 1996; Yair 1995; Hall et al. 1999; Reichman und Seabloom 2002; Hancock und Lowry 2021; Coombes 2016; Larsen et al. 2021; Corenblit et al. 2021). Previous studies estimated both positive as well as negative impacts of burrowing animals on sediment redistribution rates. The results were obtained by applying tests under laboratory conditions using rainfall simulators, conducting several field campaigns weeks to months apart, or by measuring the volume of excavated or eroded sediment in the field using methods such as erosion pins, splash boards, or simple rulers (Imeson und Kwaad 1976; Reichman und Seabloom 2002; Wei et al. 2007; Le Hir et al. 2007; Li et al. 2018; Li et al. 2019b; Li et al. 2019c; Voiculescu et al. 2019; Chen et al. 2021; Übernickel et al. 2021b; Li et al. 2019a). Although burrowing animals are generally seen as ecosystem engineers (Gabet et al. 2003; Wilkinson et al. 2009), their role in soil erosion, in general, and for numerical soil erosion models, in particular, is, to date, limited to predictions of the burrow locations and particle mixing at these locations (Black und Montgomery 1991; Meysman et al. 2003; Yoo et al. 2005; Schiffers et al. 2011). The complex interaction of sediment excavation and accumulation, and erosion processes at the burrow and hillslope scales are not yet included in the modelling, as for this, a suitable method capable of measuring all occurred redistribution processes is needed.

The reason for this knowledge gap is that previous studies have not provided data on low magnitude but frequently occurring sediment redistribution due to the specific limitations of their approaches. Field experiments with, for example, rainfall simulators can unveil processes but cannot cover the time-dependant natural dynamics of sediment redistribution. For data samplings that used methods such as erosion pins or splash boards, the sites had to be revisited each time and the data were thus obtained only sporadically (Imeson und Kwaad 1976; Hazelhoff et al. 1981; Richards und Humphreys 2010). Similarly, estimations of the excavated sediment volume are currently limited to one-time measurements or studies conducted several months apart (Black und Montgomery 1991; Hall et al. 1999; Yoo et al. 2005). We expect that non-continuously conducted measurements do not include all frequently occurring excavation and erosion processes. For this, a spatio-temporally high-resolution and continuous monitoring of sediment redistribution is needed.

High-resolution, ground-based imaging sensing techniques might overcome such aforementioned problems. Terrestrial laser scanner systems have shown to be a suitable tool for estimation of sediment redistribution and erosion processes (Nasermoaddeli und Pasche 2008; Afana et al. 2010; Eltner et al. 2016a; Eltner et al. 2016b; Longoni et al. 2016). However, they are expensive and labour-intensive. A continuous, automated monitoring of many mound areas in parallel is for this reason not possible. An already applied low-cost (up to 5000 USD) topographic monitoring technique is time-lapse photogrammetry which can be applied at variable observation distances and scales (e.g. (James und Robson 2014; Galland et al. 2016; Eltner et al. 2017; MALLALIEU et al. 2017; Kromer et al. 2019; Blanch et al. 2021). For this technique, the surface has to be monitored under various angles for which several devises are needed to be installed in the field.

In contrast, The Time-of-Flight (ToF) technology exhibits lower spatial resolution and aerial coverage compared to time-lapse photogrammetry. However, as an active remote sensing tool it can also be used at night. Additionally, the processing is less complex compared to photogrammetry because the distance values are immediately received in a local coordinate system. ToF offers here a new possibility for surface monitoring, as a technique for a cost-effective high-resolution monitoring of sediment redistribution (Eitel et al. 2011; Hänsel et al. 2016) which can be achieved by a simple installation of one device in the field. ToF-based cameras illuminate the targeted object with a light source for a known amount of time and then estimate the distance between the camera and the object by measuring the time needed for the reflected light to reach the camera sensor (Sarbolandi et al. 2018).

In our study we developed, tested and applied a cost-effective Time-of-Flight camera for automated monitoring of the rainfall and animal-driven sediment redistribution burrows and burrow embedding areas by burrowing animals with high temporal (four times a day) and spatial (6 mm) resolution. For this, we equipped several plots in remote study sites in the Chilean arid and mediterranean climate zone. We selected these sites in order to analyse sediment redistribution by burrowing activity of vertebrates under different rainfall regimes and as these sites have been shown to be particularly strongly affected by burrowing activity (Grigusova et al. 2021). We estimated the burrowing intensity and its dependence on rainfall. Then, we quantified the daily sediment redistribution within burrow and burrow embedding area. We analysed the impacts of animal burrowing activity and rainfall on the sediment redistribution and quantified the volume of sediment which is additionally incorporated to the hillslope sediment flux due to the presence of burrows. Finally, we estimated sediment redistribution on a burrow scale and upscaled sediment redistribution rates to the entire hillslopes.

2. Study area

Our study sites were located in the Chilean Coastal Cordillera in two climate zones (Fig. 1): in the National Park Pan de Azúcar (further as Pan de Azúcar or PdA) and the National Park La Campana (further as La Campana or LC). The Las Lomitas site in PdA is located in the arid climate zone of the Atacama Desert with a precipitation rate of 12 mm $year^{-1}$, and it has a mean annual temperature of 16.8 °C (Übernickel et al. 2021a). Here, the vegetation cover is below 5%, and it is dominated by small desert shrubs, several species of cacti (*Eulychnia breviflora, Copiapoa atacamensis)* and biocrusts (Lehnert et al. 2018). LC is located in the mediterranean climate zone with a precipitation rate of 367 mm $year^{-1}$ and a mean annual temperature of 14.1 °C (Übernickel et al. 2021a). LC is dominated by an evergreen sclerophyllous forest with endemic palm trees, *Jubaea chilensis*. Both research sites have a granitic rock base, and the dominating soil texture is sandy loam (Bernhard et al. 2018). In PdA, the study setup consisted of one north-facing and one south-facing hillslope. The hillslope inclinations were ~20°, and a climate station was located ~15 km from the camera sites. In LC, the setup consisted of two north-facing and one south-facing hillslopes. The hillslope inclinations were ~25°, and a climate station was located ~250 m from the south-facing hillslope (Übernickel et al. 2021a).

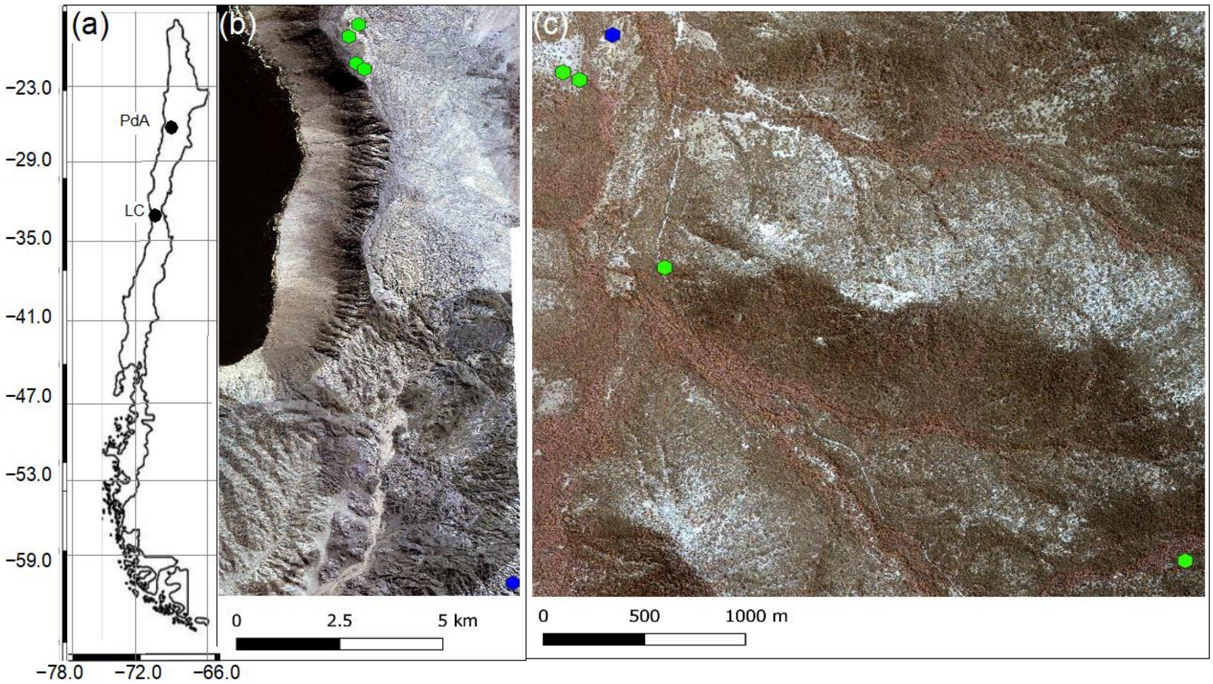

Figure 1. Location of the cameras and climate stations on which this study was based. Black points show the location of the research sites in Chile. The green points represent the camera plots, and the blue points the climate stations: (a) Location of study sites in Chile: PdA stands for Pan de Azúcar, LC for La Campana; (b) Study setup in Pan de Azúcar; (c) Study setup in LC. The background images in (b) and (c) are orthophotos created from WorldView-2 data from 19 July 2019. For exact latitude and longitude see Table A2.

2.1 Local burrowing animals

We estimated the species of the local burrowing animals by conducting a literature review and using motion-activated wildlife traps. Among the most common vertebrate burrowing animals are in PdA carnivores of the family Canidae (*Lycalopex culpaeus*, *Lycalopex griseus*); rodents of the family Abrocomidae (*Abrocoma bennetti)*, Chnichillidae (*Lagidium viscacia)*, Cricetidae (*Abrothrix andinus, Phyllotis xanthopygus*, *Phyllotis limatus, Phyllotis darwini*) and Octogontidae (Cerquiera 1985, Jimenéz et al. 1992, Übernickel et al. 2021). The most common burrowing animals in LC are carnivores of the family Canidae and Methitidae, Lagomorpha of the family Leporidae (*Oryctolagus cuniculus*), and rodents of the families Cricetidae (*Abrothrix longipilis, Abrothrix olivaceus, Phyllotis darwini*), Muridae (*Mus musculus*) and Octogontidae (*Octogon degus, Spalacopus cyanus*) (Munoz-Pedreros et al. 2018, Übernickel et al. 2021). The motion-activated traps recorded several burrowing animals: *Lycalopex culpaeus*, *Oryctolagus cunniculus* and *Abrocoma bennettii*) (Figure 2). A list of the most common local burrowing animals is shown in Table 1.

Table 1. Most common local burrowing animals. The list includes data from our motion-activated wildlife traps, and reviewe by Übernickel et al. 2021, Cerquiera 1985, Jimenéz et al. 1992, Munoz-Pedreros et al. 2018). “X” shows at which site the species can be found.

Order	**Family**	**Species**	**Common name**	**Site**	
				PdA	**LC**
Carnivora	Canidae	*Lycalopex culpaeus*	Culpeo	X	X
Carnivora	Canidae	*Lycalopex griseus*	South-American grey fox	X	X

Carnivora	Methitidae	*Conepatus chinga*	Molina's Hog noised skunk		X
Lagomorpha	Leporidae	*Oryctolagus cuniculus*	European rabbit		X
Rodentia	Abrocomidae	*Abrocoma bennetti*	Bennett's chinchilla rat	X	X
Rodentia	Chinchillidae	*Lagidium viscacia*	Southern mountain vischacha	X	
Rodentia	Cricetidae	*Abrothrix andinus*	Andean grass mouse	X	
Rodentia	Cricetidae	*Abrothrix longipilis*	Long-haired mouse	X	X
Rodentia	Cricetidae	*Abrothrix olivaceus*	Olive grass mouse	X	X
Rodentia	Cricetidae	*Phyllotis darwini*	Darwin's leaf-eared mouse	X	X
Rodentia	Cricetidae	*Phyllotis xanthopygus*	Yellow leaf-eared mouse	X	
Rodentia	Cricetidae	*Phyllotis limatus*	Lima leaf-eared mouse	X	
Rodentia	Muridae	*Mus musculus*	Common house mouse	X	X
Rodentia	Octogontidae	*Octogon degus*	Degu (rat)	X	X
Rodentia	Octogontidae	*Spalacopus cyanus*	Coruro (rat)	X	X

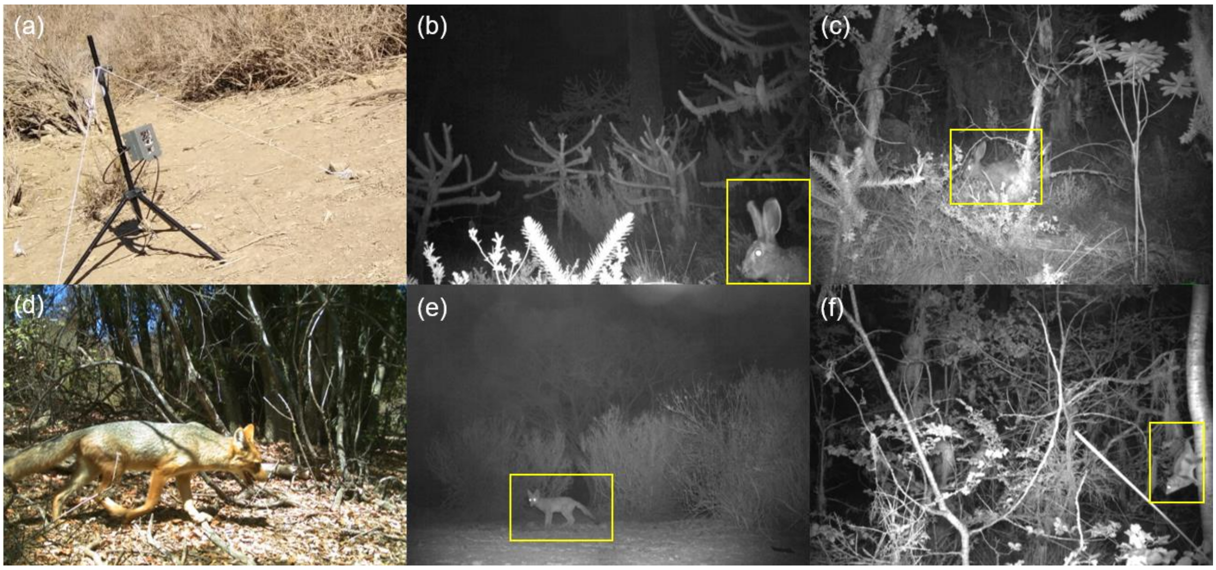

Figure 2. Examples of local burrowing animals obtained by motion-activated traps. (a) Motion-activated camera trap. (b) and (c) European rabbit (*Oryctolagus cunniculus*). (d) and (e) Culpeo (*Lycalopex culpaeus*). (f) Bennett's chinchilla rat *(Abrocoma bennettii)*. The yellow circle indicates the position of the animal on the photo. Photos by Diana Kraus.

3. Methodology

3.1 Time-of-Flight (ToF) principle

A Time-of-Flight-based camera illuminates an object with a light source, usually in a non-visible spectrum, such as near-infrared, for a precise length of time. ToF cameras rely on the principle of measuring the phase shift, with different options to modulate the light source to be able to measure the phase shift. The here employed cameras used pulse-based modulation, meaning the light pulse was first emitted by the camera, then reflected from the surface, and finally measured by the camera using two temporary windows. The opening of the first window is synchronized with the pulse emission i.e. the receiver opens the window with the same Δt as the emitted pulse. Then, the second window is opened, for the same duration Δt, which is synchronised with the closing of the first window. The first temporary window thus measures the incoming reflected light while the light pulse is also still emitting from the camera. The second temporary window measures the incoming reflected light when no pulse is emitting from the camera. The captured photon number (i.e. measured by electrical charge) in both windows can be related according to equation 1 and the distance from the camera to the object can then be calculated as follows:

$$d = \frac{1}{2} * c * t * \left(\frac{g1}{g1+g2}\right) \quad . \qquad (1)$$

In Eq. (1), d (m) is the distance from the camera to the object, c (m s^{-1}) is the speed of light (299,792,458 m s^{-1}), t (s) is the overall time of the illumination and measurement, g_1 is the ratio of the reflected photons to all photons accumulated in the first window, and g_2 the ratio of the reflected photons to all photons accumulated in the second window (Sarbolandi et al. 2018; Li 2014).

The sensor in our camera came from Texas Instruments and the data scan contained information on 320 x 240 points. The camera field of view (FOV) and the spatial resolution of the scans depended on the height of the camera above the surface and camera orientation. The distance was calculated for every point, and the object was saved in binary format as a collection of 3D points with *x*-, *y*- and *z*-coordinates. The point clouds taken by the camera were transformed from the binary format to an ASCII format. Each point in the point cloud was assigned to an *x*-, *y*- and *z*-coordinate. The coordinates were distributed within a three-dimensional Euclidian space, with the point at the camera nadir (the centre of the camera sensor) being the point of origin of the 3D Cartesian coordinate system. *x*- and *y*-coordinates describe the distance to the point of origin (m). *z*-coordinate describes the distance (m) from the object to the camera. The lowest point of the scanned surface thus has the highest *z*-coordinate value.

3.2 Data processing

The distortion caused by the hillslope and the camera angle was corrected for each point cloud as follows:

$$z_{cor} = z_{uncor} - \tan(\alpha + \beta) * (y_1 - y_i) \quad . \qquad (2)$$

In Eq. (2), z_{cor} is the corrected distance (m) between the camera and surface (m), z_{uncor} is the uncorrected *z*-coordinate (m), α is the tilt angle of the camera (°), β is the surface inclination (°), and y_i (m) is the distance between each point, and the point with i) an y-coordinate = 0 and ii) the same x-coordinate as the respective point. The most frequent errors were identified and treated as follows. Due to the ambient light reaching the camera sensor, the *z*-coordinate values of some of the points were incorrect (scattering error). To remove this error, a threshold value was calculated for each point cloud:

$$\Omega = mean_{zcor-coordinates} \pm sd_{zcor-coordinates} \quad . \qquad (3)$$

In Eq. (3), Ω is the threshold value, $mean_{zcor-coordinate}$ is the average value, and $sd_{zcor-coordinate}$ is the standard deviation of the corrected *z*-coordinates (m). Then, all points with a *z*-coordinate above and below this value were deleted. Point clouds with more than 50% of points above the threshold value Ω were also not considered for further processing. A drift error occurred when the *z*-coordinate values of around one-third of the point clouds decreased by several centimetres from one point cloud to another. Here, the average *z*-coordinate of ten point clouds before and after the drift were calculated, and the difference was added to *z*-coordinates of the points affected by the drift. The corrected height values were then transformed into a digital surface model (DSM).

3.3 Accuracy of the ToF cameras

The accuracy of the ToF camera was tested under laboratory conditions by recreating similar surface conditions as in the field (sloping surface, covered by sediment). An artificial mound using sediment extracted from a riverbank in central Germany was used, mimicking a mound created by a burrowing animal. During the test, the camera was installed 100 cm above the surface. The camera FOV was 3 m^2 and the scan spatial resolution was 6 mm. The surface was scanned twice by the ToF camera. Then 100 – 450 cm^3 of sediment was manually extracted from the mound. The volume of the extracted sediment was measured by a measuring cup. After extraction, the surface was again scanned twice by the camera. The experiment was repeated 45 times with varying amounts of extracted sediment. The scans were transformed to point clouds in VoxelViewer-0.9.10, and the point clouds were corrected according to Eq. (2) and (3). The *z*-coordinates of the two point clouds before and two point clouds after the extraction were averaged. The standard deviation of the z-coordinate of the two scans was 0.06 cm. Figure A1 shows the spatially distributed standard deviation. The deviation increases from the centre towards the corners of the scan. The mound was outlined and only the points representing the mound were used in the further analysis. The point clouds were then transformed into DSMs, and the differences between the time steps were calculated. A scan was taken of a smooth surface (linoleum floor) and a point cloud was created from the data. Then, we fitted a plane into the point cloud and calculated the distance between the plane and the camera sensor. The standard variation (0.17 cm) in the distance measurements was saved. Solely, the differences between the DSMs below this variation were considered in the calculation of the detected sediment extraction. The detected extracted sediment volume was then calculated for each experiment as follows:

$$Vol_{detected} = \sum_{p}^{1}\left(DSM_{before} - DSM_{after}\right) * \ res^2 \quad , \qquad (4)$$

In Eq. (4), $Vol_{detected}$ is the volume of the extracted sediment as detected by the camera (cm^3), p is the number of pixels, DSM_{before} (cm) is the DSM calculated from the scan taken before the extraction, DSM_{after} (cm) is the DSM calculated from the scan taken after the extraction, res (cm) is the resolution of the scan, which was 0.6 cm. To evaluate the camera's accuracy, the measured volume of the extracted sediment was compared to the volume detected by the camera. The camera's accuracy was estimated between the detected volume and measured volume as follows:

$$MAE = \sum_{1}^{n} \frac{(Vol_{detected} - Vol_{measured})}{area} \quad . \qquad (5)$$

In Eq. (5), MAE (cm^3/cm^2) is the mean absolute error, n is the number of scans, $Vol_{measured}$ (cm^3) is the volume of the extracted sediment measured by the measuring cup, and the area is the total surface area monitored by the camera (cm^2).

3.4 Installation of the cameras in the field

We installed 8 custom-tailored ToF-based cameras on 4 hillslopes in two climate zones in areas including visible signs of bioturbation activity (burrows) and areas without visible signs of bioturbation (Fig. 3). The cameras were installed in LC on the north-facing upper hillslope (LC-NU), north-facing lower hillslope (LC-NL), south-facing upper hillslope (LC-SU) and the south-facing lower hillslope (LC-SL); in PdA on the north-facing upper hillslope (PdA-NU), north-facing lower hillslope (PdA-NL), south-facing upper hillslope (PdA-SU) and south-facing lower hillslope (PdA-SL). The custom-tailored cameras were installed during a field campaign in March 2019, the monitoring took place for seven months, and the data were collected in October 2019. The construction consisted of a 3D ToF-based sensor from Texas Instruments (Li, 2014), a RasperryPi single board computer (SBC), a timer, a 12 V 12 Ah battery and three 20 W solar panels for unattended operation (Fig. 2). Solar panels were located at the camera pole and were recharging the battery via a charge controller. The camera was located approximately one meter above the surface, facing the surface with a tilt angle of 10 degrees. The timer was set to close the electric circuit 4 times a day: at 1 a.m., 5 a.m., 8 a.m. and 10 p.m. At these times, the camera and the computer were turned on for 15 minutes. The camera turned on and took five scans delayed one second from each other and sent them to the SBC. Each camera had its own WiFi (Wireless Fidelity) and the data could be read from the SBC via Secure Shell (SSH). The cameras collected the data for the time period of 7 months.

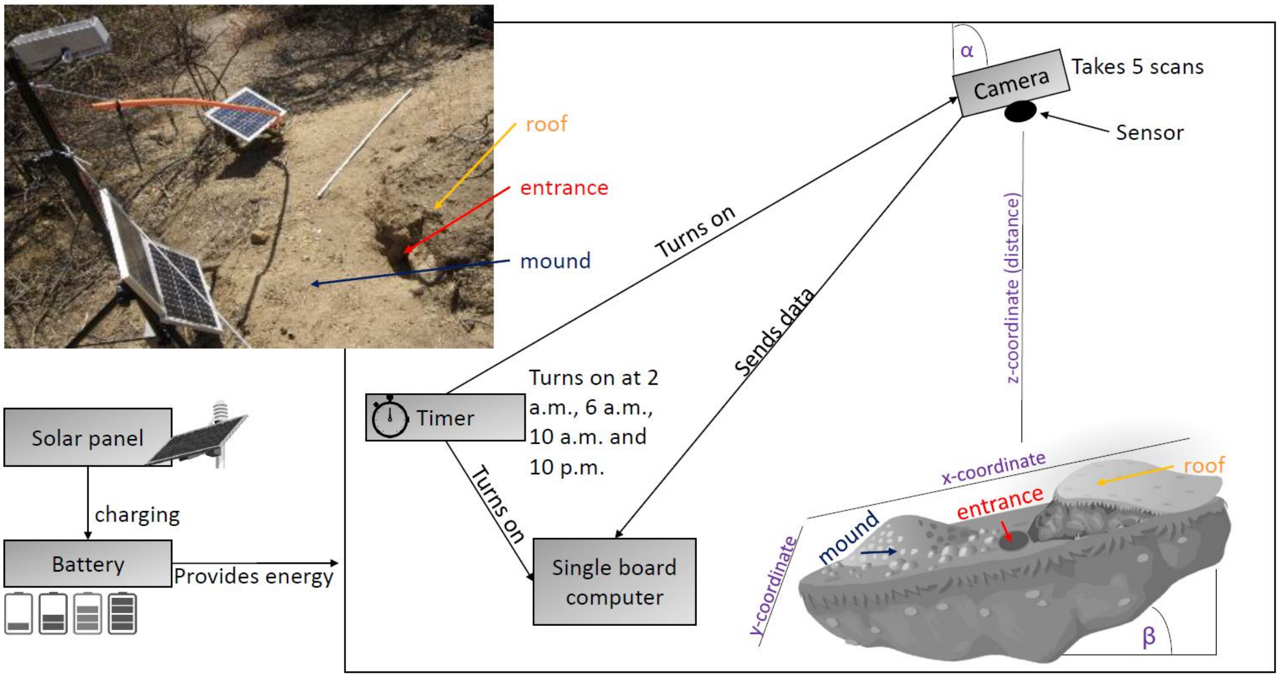

Figure 3. Scheme and photo example of a Time-of-Flight-based camera installation in the field. The photo example is from upper north-facing hillslope in La Campana. Black boxes describe single installation parts. Purple descriptions are the variables needed for the correction of the scans. Roof, entrance and mound describe parts of the burrow. The *x*-, *y*- and *z*-coordinates are 3D coordinates identifying the position of each point in space, where the *x*-coordinate is the length, *y*-coordinate is the width and the *z*-coordinate is the distance between the camera sensor and the surface. α is the inclination of the camera, and β is the surface inclination.

3.5 Delineation of burrows and burrow embedding areas

The surface area scanned by the cameras was divided by a delineation scheme into burrows (B) and burrow embedding areas (EM). The burrows included three sub-areas: (i) mound (M), (ii) entrance (E) and (iii) burrow roof (R). “Mound” describes the sediment excavated by the animal while digging the burrow. “Entrance” describes the entry to the animal burrow up to the depth possible to obtain via the camera. “Burrow roof” describes the part of the sediment above and uphill the burrow entrance (BANCROFT et al. 2004). During the burrow’s creation, sediment was not only excavated but also pushed aside and uphill the entrance, which created the burrow roof. We assume that this elevated microtopographical feature then forms an obstacle for sediment transported from uphill, which leads to its accumulation in this area. The remaining surface within the camera's FOV was burrow embedding area. Please note, that this area may still be affected by the burrowing activity of the animal and is not completely unaffected by the animal.

For the delineation, we used the DSM calculated from the point cloud, and a slope layer calculated from the DSM (Horn 1981). The DSM had a size of 4 m^2 a resolution of 0.6 cm. Entrance was assigned to an area determined by a search algorithm starting at the lowest point of the DSM (pixel with the highest *z*-coordinate value). We increased the circular buffer around the starting point by one pixel until the average depth of the new buffer points was not higher than the height of the camera above the surface, or until the slope of at least 50% of the new buffer points was not 0. Then, we masked all pixels within the buffer with a depth lower than the average depth of the points within the buffer, which had a slope that was 0. The remaining pixels belonged to the entrance area. Then, the surface scan was divided into an uphill and downhill part with regards to the entrance position. Both the uphill and the downhill parts were subdivided into 16 squares, so that each of the four quadrants within the 2D grid (x- and y-axis) contained four squares. The squares had size of 0.5 m^2.

To delineate the mound in the downhill part, we first identified the highest points (pixel with the lowest *z*-coordinate value) within all 16 squares. We then calculated the distance of these maxima to the entrance, and the pixel located nearest to the entrance was identified as the highest point of the mound (i.e., seed point). Consecutively, we increased the circular buffer around the seed point by one pixel until the average depth of the new buffer points was not lower than the height of the camera above the surface, or until the slope of at least 50% of the new buffer points was not 0. Then, we masked all pixels within the buffer with a depth higher than the average depth of the points within the buffer, which had a slope that was 0. The remaining pixels were classified as mound area. To delineate burrow roof, we used the same approach as for the delineation of mound and applied it on the uphill part of the surface scan. We used the DEM and slope layers for the delineation for several reasons. The distance from the surface to the camera was the most important parameter to derive (i) the deepest point of the entrance and (ii) the highest point of the mound or burrow roof, as this was (mostly) the closest point to the camera. After the angle correction of the z-coordinate according to chapter 3.2., the surface inclination of the areas without burrow was 0°, while the angle between the border of the burrow entrance or mound and the burrow embedding surface was above 0°. Because neither the entrance nor the mound have a perfect circular form, we would largely overestimate or underestimate the entrance or mound size. Overestimate by not stopping the search algorithm until the angle between all new points of the buffer to the rest of the buffer was 0°. Underestimate by stopping the algorithm when the angle of one point of the buffer to the nearest point of the buffer was 0°. The value of 50% thus minimized the error. All pixels that were not classified during the entire delineation process were treated as burrow embedding areas.

The position and the boundaries of entrance, mound and burrow roof were validated visually (Fig. 4 and A2).

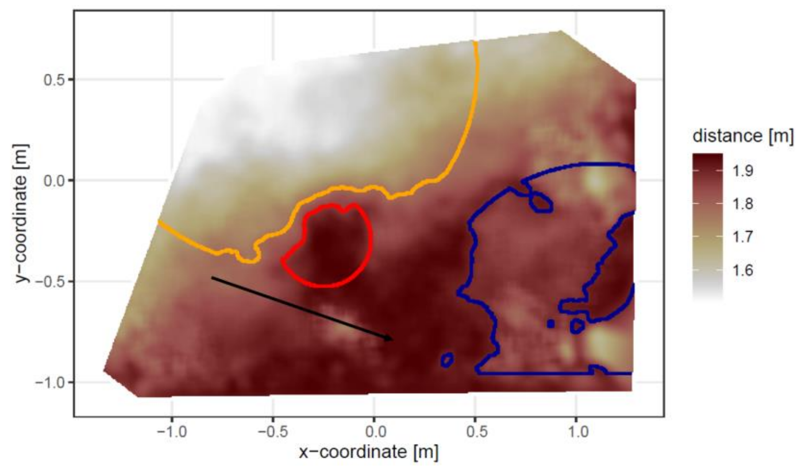

Figure 4. Corrected digital surface model of the camera on the upper north-facing hillslope in La Campana with delineated areas. The point of origin of the coordinate system is at the camera nadir. Distance refers to the distance between surface and camera. The red line delineates the burrow entrance, blue the mound and orange the burrow roof. The area which was outside of any delineated area was classified as burrow embedding area. The arrow indicates a downhill direction of the hillslope.

In LC, the burrows always consisted of an entrance, mound and burrow roof. In PdA, there was no burrow roof on the upper hillslopes. Burrows without a burrow roof were located on shallower parts of the hillslopes (up to an inclination of 5°), and the angle of the burrow entrance to the ground was ~90°. Burrows with a burrow roof were located on steeper parts of the hillslopes (with an inclination above 5°), and the angle of the burrow entrance to the ground was ~45°.

3.6 Calculation of animal-caused and rainfall-caused sediment redistribution

We pairwise compared the DSMs of each scan with the scan saved before and identified 3 types of sediment redistribution which occurred in the time period between these images. The 3 types of redistribution were: a) animal caused; b) rainfall-caused; c) both animal and rainfall caused.

The animal-caused sediment redistribution occurred when the animal actively reworked sediment within its burrow. Following five prerequisites had to be met when the sediment redistribution was caused solely by the animal: (i) as the animal excavates sediment from the entrance, the depth of the entrance must increase in the second scan; (ii) as the excavated sediment accumulates on the mound, the height of the mound must increase in the second scan; (iii) as the burrowing might lead to an expansion or a collapse of the burrow roof, an increase or decrease of the burrow roof must occur between the scans; (iv) as the animal only digs within his burrow, no changes must occur between the two scans within the burrow embedding area by the animal; (v) no rainfall occurred during this period.

The rainfall-caused sediment redistribution was calculated as follows: From the data from the climate stations (Übernickel et al. 2021a), we calculated the daily precipitation in mm. The sediment redistribution recorded immediately and within five scans before and after a rainfall event is defined to be the result of the rainfall event. This was necessary as the climate stations are located up to a 15 km distance from the cameras (Fig. 1). To attribute sediment redistribution to rainfall event, three preconditions had to be met: (i) A rainfall event occurred; (ii) sediment is eroded from burrow roof, mound and the embedding area; (iii) sediment is accumulated within the burrow entrance.

To attribute sediment redistribution to a combination of animal activity and rainfall, four preconditions had to be met: (i) A rainfall event occurred; (ii) sediment is eroded from embedding area; (iii) the height of burrow roof and mound decreased or increased; (iv) the depth of burrow entrance increased.

The animal-caused sediment redistribution was calculated as the sediment volume excavated from the entrance. Animal excavation always increased depth of the burrow entrance. The rainfall-caused sediment redistribution was calculated as the sediment volume which eroded from the burrow roof and mound. During a rainfall event, sediment eroding from burrow roof might accumulate within burrow entrances. In this case, the depth of the burrow entrance decreased. No sediment could erode from the entrance during a rainfall event. Decreased depth of a burrow entrance always points to sediment redistribution caused by rainfall, increased depth of burrow entrance always means redistribution by animals. Rainfall-caused redistribution always occurred before animal-caused redistribution, as without erosion caused by rainfall, the animals did not need to reconstruct their burrows.

3.7 Calculation of daily sediment mass balance budget

The volume of the redistributed sediment was calculated daily and was then cumulated from the first day of monitoring. For the calculation of the daily sediment redistribution, the change in the surface level detected by the camera was calculated first. For each day, the scans from the day before and after the respective day were averaged and subtracted. The average standard deviation of the z-coordinate of these scans was 0.06 cm. As described in Section 2.2., all values with a difference below and above the threshold value of 0.2 cm were set to 0. The redistributed sediment volume was then calculated from the surface change for each pixel as follows:

$$Vol_{redistributed} = (S_b - S_a) * res^2 \quad . \tag{6}$$

In Eq. (6), $Vol_{redistributed}$ (cm^3 pixel^{-1}) is the volume of the calculated redistributed sediment, S_b (cm) the scan before, S_a (cm) the scan after the rainfall event and *res* is the spatial resolution (cm). Using the daily volume of the redistributed sediment per pixel, we calculated the daily mass balance budget by summing the volume of sediment eroding or accumulating within each delineated area.

3.8 Calculation of the overall volume of redistributed sediment after the period of 7 months

From the camera data, we calculated the average cumulative volume of redistributed sediment for the period of 7 months within burrows ($Vol_{burrows}$ (cm^3 cm^{-2} year^{-1})) and burrow embedding ($Vol_{embedding}$ (cm^3 cm^{-2} year^{-1})) areas and the average sediment volume redistributed (excavated) by the animal (Vol_{exc} (cm^3 cm^{-2} year^{-1})), separately for each site. We estimated the volume of sediment that was redistributed during rainfall events due to the presence of the burrow (Vol_{add} (cm^3 cm^{-2} year^{-1})). Vol_{add} was calculated as the difference in the redistributed sediment volume between burrows and burrow embedding areas according to Eq. (7).

$$Vol_{add} = \left(Vol_{affected} - Vol_{unaffected}\right) * 1.71 \quad , \tag{7}$$

Additionally, we calculated the average volume of the redistributed sediment per burrow ($Vol_{per\ burrow}$ [cm^3 burrow^{-1} year^{-1}]).

$$Vol_{per\ burrow} = (Area_{burrow} * Vol) * 1.71 \tag{8}$$

In Eq. (8), $Area_{burrow}$ (cm^2) is the average size of the burrows that are monitored by the cameras; Vol is Vol_{burrow} (cm^3 cm^{-2} year^{-1}), Vol_{exc} (cm^3 cm^{-2} year^{-1}) or Vol_{add} (cm^3 cm^{-2} year^{-1}).

We then upscaled the Vol_{burrow} (cm^3 cm^{-2} year^{-1}), Vol_{exc} (cm^3 cm^{-2} year^{-1})) and Vol_{add} (cm^3 cm^{-2} year^{-1})) to the hillslope using the following approach. Hillslope-wide upscaling of the results generated in this study was performed by using a previous estimation of vertebrate burrow density (Grigusova et al. 2021). In this study, the density of burrows was measured in situ within eighty 100 m^2 plots and then upscaled to the same hillslopes on which the cameras were located by applying machine-learning methods, using the UAV-data as predictors. For upscaling, we applied a random forest model with recursive feature elimination. The model was validated by a repeated Leave-One-Out cross validation. The density of vertebrate burrows was between 6 and 12 100 m^2 in LC and between 0 and 12 100 m^{-2} in Pan de Azúcar. Using the hillslope-wide predicted vertebrate burrow densities ($Dens_{burrow}$ (number of burrows 100 m^{-2})) from Grigusova et al. 2021, we estimated the volume of redistributed sediment for each pixel of the raster layers ($Vol_{per\ pixel}$ ($cm^3\ m^{-2}\ year^{-1}$)) according to Eq. (9):

$$Vol_{per\ pixel} = Vol_{per\ burrow} * \ Dens_{burrow} * 1.71 \qquad (9)$$

The average hillslope-wide volume of redistributed sediment ($Vol_{hillslope\text{-}wide}$ ($m^3\ ha^{-1}\ year^{-1}$)) was then estimated as follows:

$$Vol_{hillslope-wide} = \sum_1^m Vol_{\ per\ pixel} \ * 0.001 * 1.71 \quad , \qquad (10)$$

In Eq (10), m is the number of pixels.

4. Results

4.1 Camera accuracy and data availability

The accuracy between the measured extracted sediment volume and sediment volume calculated from the camera scans was very high (MAE = 0.023 $cm^3\ cm^{-2}$, R^2 = 0.77, SD = 0.02 $cm^3\ cm^{-2}$, Fig. A3). The accuracy between the calculated and measured extracted sediment was higher when the two scans taken before as well as after the extraction of the sediment were averaged and the sediment volume was estimated using these averaged scans. When calculating the redistributed sediment from solely one scan before and after extraction, the accuracy slightly decreased (MAE = 0.081 $cm^3\ cm^{-2}$, R^2 = 0.64). The cameras tended to overestimate the volume of redistributed sediment. Six out of eight custom-tailored cameras collected data over the seven-month period (Table A2). One camera collected data for a period of three months and one camera stopped working a few days after installation. The quantity of usable point clouds taken at 1 a.m., 5 a.m. and 10 p.m. was higher than of point clouds taken at 8 a.m. Approximately 20% of points was removed from the point clouds before final analysis due to the high scattering at the point cloud corners. After data filtering (see Section 3.2.), 1326 scans were usable and for 86% of the days, at least one usable scan was available. The usable scans were distributed continuously within the monitoring period.

4.3 Mass balance of redistributed sediment

The cameras detected (i) sediment redistribution directly following rainfall events and (ii) due to the burrowing activity in times without rainfall (Fig. 5, A4 and A5). In all cases, burrows (entrance, burrow roof and mound) exhibited higher sediment redistribution rates than burrow embedding areas. In addition, the volume of redistributed sediment by animal activity was higher after a rainfall event occurred.

In the following, the dynamics are exemplary explained for four cameras. Animal burrowing activity was detected seven times by the camera LC NU (Fig. 5a, A4, A5) during the monitoring period, by an increase in sediment volume in the area delineated as mound. Simultaneously, the burrow entrance showed signs of modification and sediment accumulation, but these changes were less clear. Overall, the volume of the excavated soil varied. From April until June, up to 0.5 $cm^3\ cm^{-2}$ of sediment was excavated by the animal and accumulated on the mound. From June until September, animal burrowing activity was detected at four time slots (5 June 2019, 9 June 2019, 1 July 2019 and 18 August 2019) and sediment volume of up to 2 cm^3 cm^{-2} accumulated each time on the mound, burrow roof and within the entrance. During the rainfall events of up to 20 mm day^{-1} on 16 June 2019, 27 mm day^{-1} on 29 June 2019 and 7 mm day^{-1} on 13 July 2019, sediment volume of up to 4 cm^3 cm^{-2} eroded, especially from the burrow roof and the mound while a sediment volume of up to 1 cm^3 cm^{-2} accumulated within the entrance during each rainfall event. Camera LC-SL (Fig. A4, A5) showed burrowing activities eight times and sediment volumes of up to 3 cm^3 cm^{-2} accumulated within the entrance and burrow roof. The camera detected sediment erosion of up to 2 cm^3 cm^{-2} after a rainfall event of 27 mm day^{-1} on 27 July 2019. On the south-upper hillslope, the camera detected animal burrowing activity six times, with a sediment accumulation of up to 3 cm^3 cm^{-2} (Fig. A2 and A3).

In contrast, camera PdA-NU pointed to animal burrowing activity up to 15 times where up to 1 cm^3 cm^{-2} of sediment volume was redistributed from the entrance to the mound (Fig. 5b, A4, A5). At the end of June on 27 June 2019, a rainfall event of 1.5 mm day^{-1} occurred and up to 2 cm^3 cm^{-2} of sediment eroded from the burrow roof and accumulated within the burrow entrance. We observed increased sediment redistribution by the animal after the rainfall events. Camera PdA-SL evenly revealed animal burrowing activity up to 15 times ((Fig. A4, A5)). The burrowing had a strong effect on the sediment redistribution. The rainfall event of 1.5 mm day^{-1} on 27 June 2019 did not cause any detectable surface change.

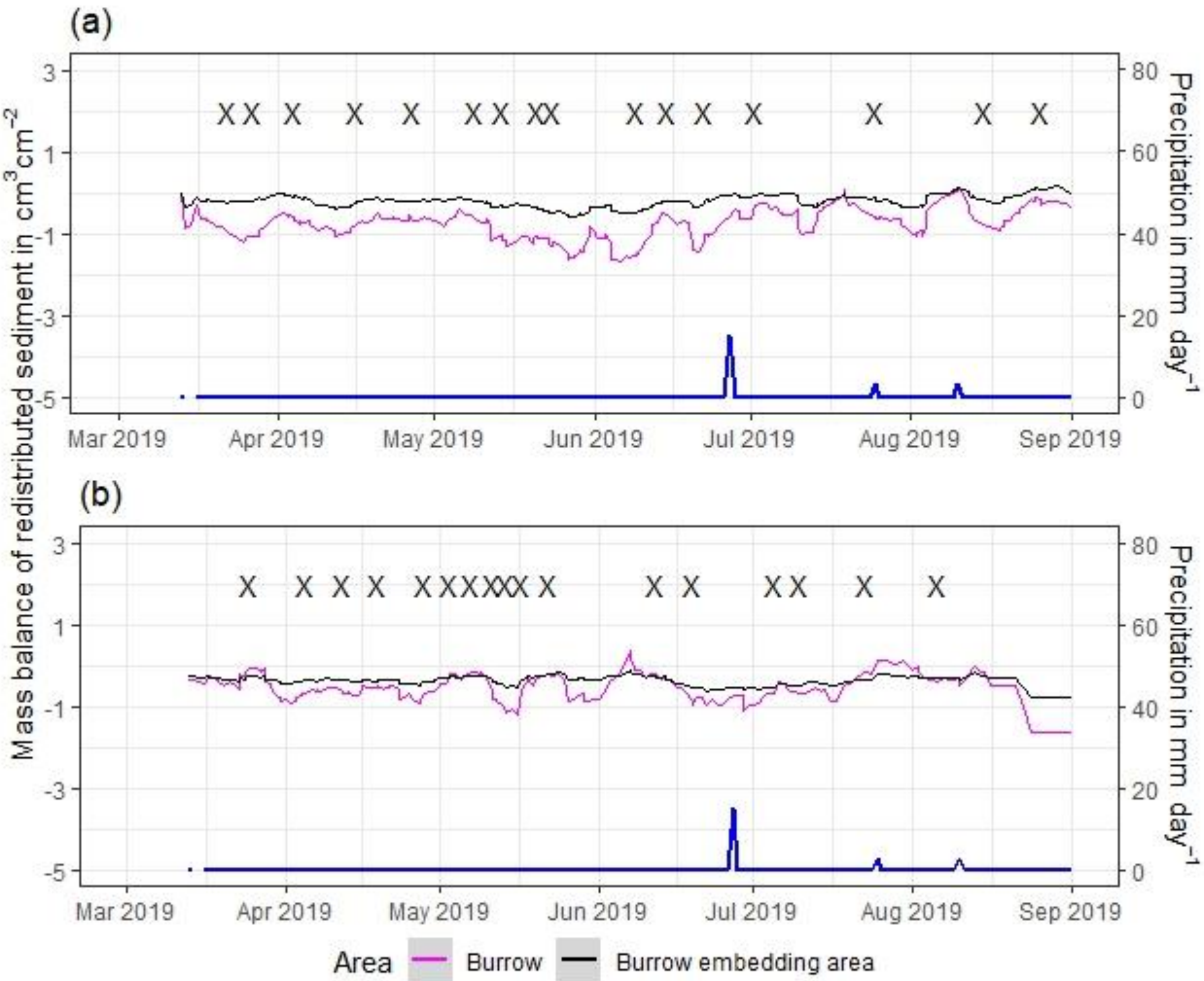

Figure 5. Examples of the mass balance of redistributed sediment for burrows and burrow embedding areas (**a**) The record of the camera on the upper north-facing hillslope in La Campana showed that larger rainfall

events cause a negative sediment balance (sediment loss), followed by a phase of positive sediment mass balance after approximately 3 days due to sediment excavation; (**b**) The record of the camera on the upper north-facing in Pan de Azúcar hillslope showed a similar pattern to the camera on the upper north-facing hillslope, but the phase of positive mass balance was delayed in comparison. The blue line is the daily precipitation in mm day^{-1}, and “X” marks the days at which animal burrowing activity was detected. Mass balances for all cameras are displayed in Fig. A2 and A3.

The analysis of cumulative volume of the redistributed sediment caused by burrowing animal activity and rainfall over the monitored period of seven months for all eight cameras showed a heterogeneous pattern.

In LC, the cumulative volume of the sediment excavated by the animal within the burrow roof and mound increased continuously (Fig. 6, A7). Especially between the rainfall events from June until August, a cumulative volume of on average 6.5 cm^3 cm^{-2} was excavated by the animal. We calculated that, on average, 8.53 cm^3 cm^{-2} cumulatively eroded from the burrow roof and mound; while 2.44 cm^3 cm^{-2} sediment volume accumulated within the entrance (Fig. 6, A7). These results indicate that 28% of sediment eroding from the burrow roof accumulated within the entrance, while over 62% of sediment eroded downhill. Averaged over all camera scans, 338% more sediment was redistributed by rain within burrow compared to the burrow embedding area (Fig. 7).

In PdA, cameras continuously detected animal burrowing activity and excavation of the sediment (Fig. A7). The volume of the detected excavated sediment increased steadily within all cameras. The cumulative sediment accumulation surpasses the sediment eroded due to the rainfall. The volume of the sediment eroded within the burrows was 40% higher than within the burrow embedding areas. The results show that approximately 50% of the eroded sediment accumulated within the entrance (Fig. 7).

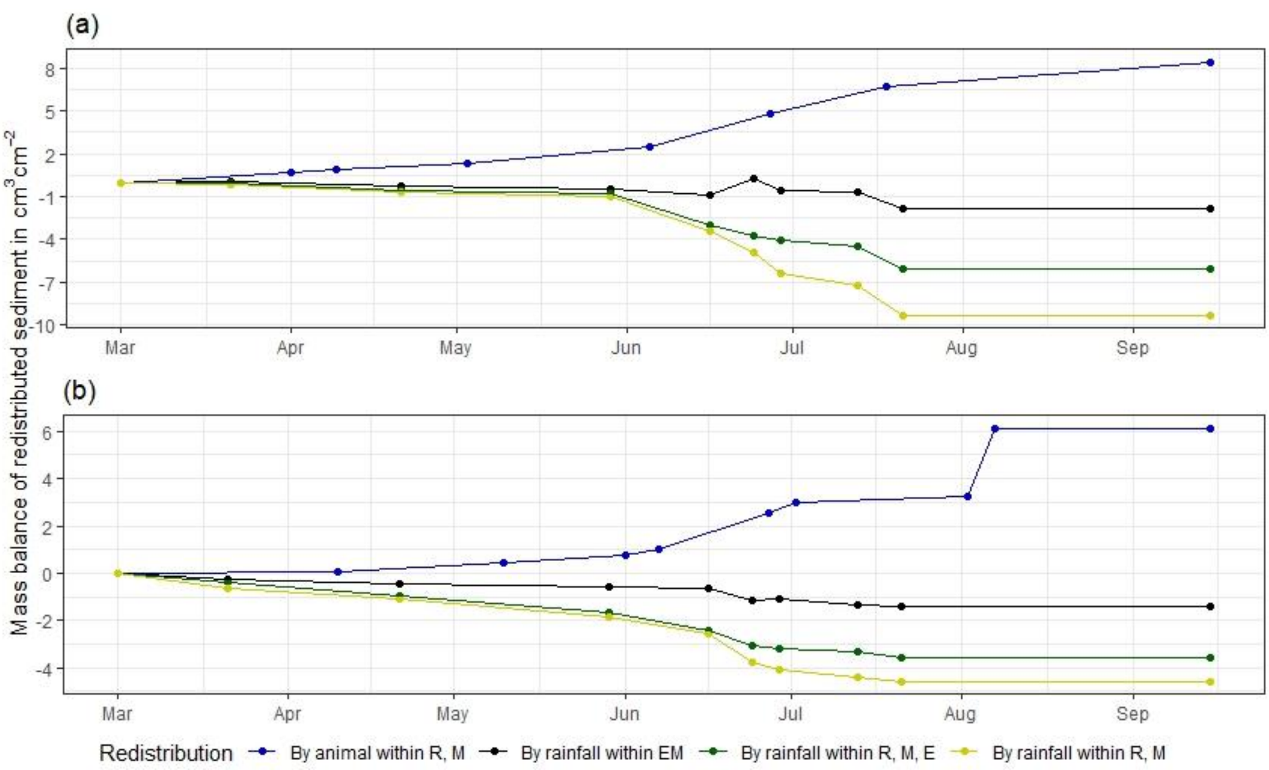

Figure 6. Examples of the cumulative volume of redistributed sediment within burrows and burrow embedding areas caused by animal burrowing activity or rainfall in mediterranean La Campana: (**a**) Upper north-facing

hillslope; (**b**) Lower south-facing hillslope. Positive values indicate sediment accumulation. Negative values indicate sediment erosion. E is the burrow entrance; M is the mound; R is burrow roof; EM is the burrow embedding area. Cumulative volumes for all cameras are in Fig. A7.

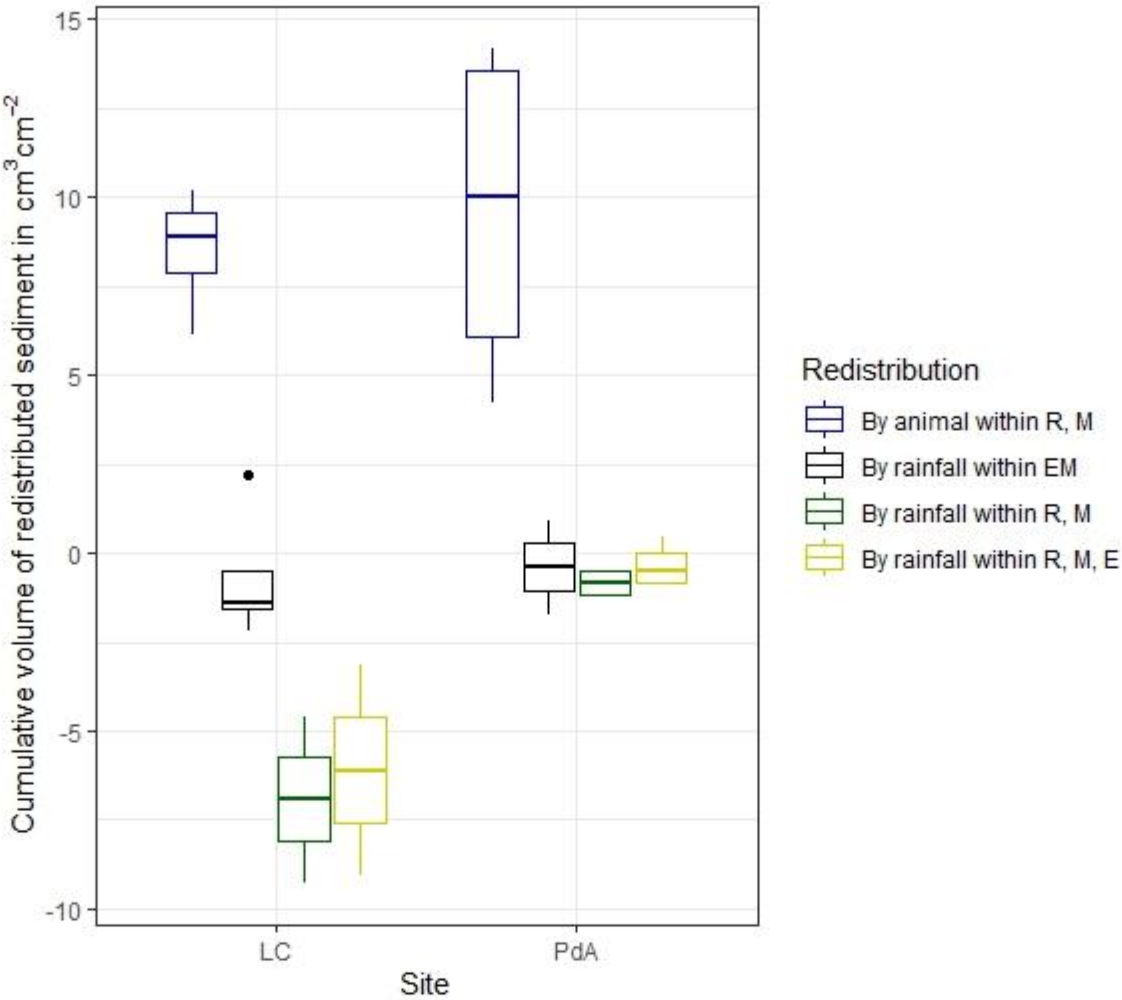

Figure 7. Cumulative volume of the redistributed sediment for all cameras. Positive values indicate sediment accumulation. Negative values indicate sediment erosion. Whiskers indicate the median of sediment redistribution. E is the burrow entrance; M the mound; R is the burrow roof; EM is burrow embedding area; LC stands for National Park La Campana in the mediterranean climate zone; PdA stands for National Park PdA in the arid climate zone.

4.4 Volume of redistributed sediment

The average size of the burrows was 84.36 cm^2 (SD = 32.54 cm^2) in LC and 91.35 cm^2 in PdA (SD = 8.53 cm^2). The animals burrowed on average 1.2 times month^{-1} in LC and 2.33 times month^{-1} in PdA. The volume of the excavated sediment was 102.22 cm^{-3} month^{-1} in LC and 124.89 cm^3 month^{-1} in PdA. Each time the animals burrowed, they excavated 42 cm^3 sediment volume in LC and 14.33 cm^3 sediment volume in PdA. The burrowing intensity increased in winter after the rainfall occurrences in LC and stayed constant during the whole monitoring period in PdA. The burrows deteriorate after rainfall events with a rate of 73.03 cm^3 month^{-1} or 63.90 cm^3 event^{-1} in LC and 10.53 cm^{-3} month or 24.57 cm^3 event^{-1}.

The overall volume of the sediment excavated by the animal and redistributed during rainfall events varied between the sites (Table 1). The volume of the sediment redistributed by the animal was lower in LC than in PdA. However, on the hillslope scale, a higher total area-wide volume of excavation was calculated for LC compared to PdA, due to the higher burrow density in LC. The volume of the sediment redistributed within burrows during rainfall events was higher in LC than in PdA. The volume of additionally redistributed sediment due to the presence of burrows was higher in LC than in PdA (Table 2, Fig. 8).

Table 2. Summary of the volume of redistributed sediment, according to area and disturbance type. Vol_{exc} describes volume of the sediment excavated by the animals. Vol_{burrow} describes volume of the sediment redistributed during rainfall events within burrows. Vol_{add} describes the difference in redistributed sediment volume within burrows and burrow embedding areas during rainfall.

Disturbance	Area	PdA	LC
Vol_{exc}	Affected area	16.41 cm^3 cm^{-2} $year^{-1}$	14.62 cm^3 cm^{-2} $year^{-1}$
	Per burrow	1498.66 cm^3 $burrow^{-1}$ $year^{-1}$	1226.61 cm^3 $burrow^{-1}$ $year^{-1}$
	Hillslope-wide	0.18 m^3 ha^{-1} $year^{-1}$	0.67 m^3 ha^{-1} $year^{-1}$
$Vol_{affected}$	Affected area	-1.97 cm^3 cm^{-2} $year^{-1}$	-10.44 cm^3 cm^{-2} $year^{-1}$
	Per burrow	-126.36 cm^3 $burrow^{-1}$ $year^{-1}$	-876.38 cm^3 $burrow^{-1}$ $year^{-1}$
	Hillslope-wide	-0.05 m^3 ha^{-1} $year^{-1}$	-0.48 m^3 ha^{-1} $year^{-1}$
Vol_{add}	Affected area	-1.18 cm^3 cm^{-2} $year^{-1}$	-7.37 cm^3 cm^{-2} $year^{-1}$
	Per burrow	-48.36 cm^3 $burrow^{-1}$ $year^{-1}$	-619.2 cm^3 $burrow^{-1}$ $year^{-1}$
	Hillslope-wide	-0.02 m^3 ha^{-1} $year^{-1}$	-0.34 m^3 ha^{-1} $year^{-1}$

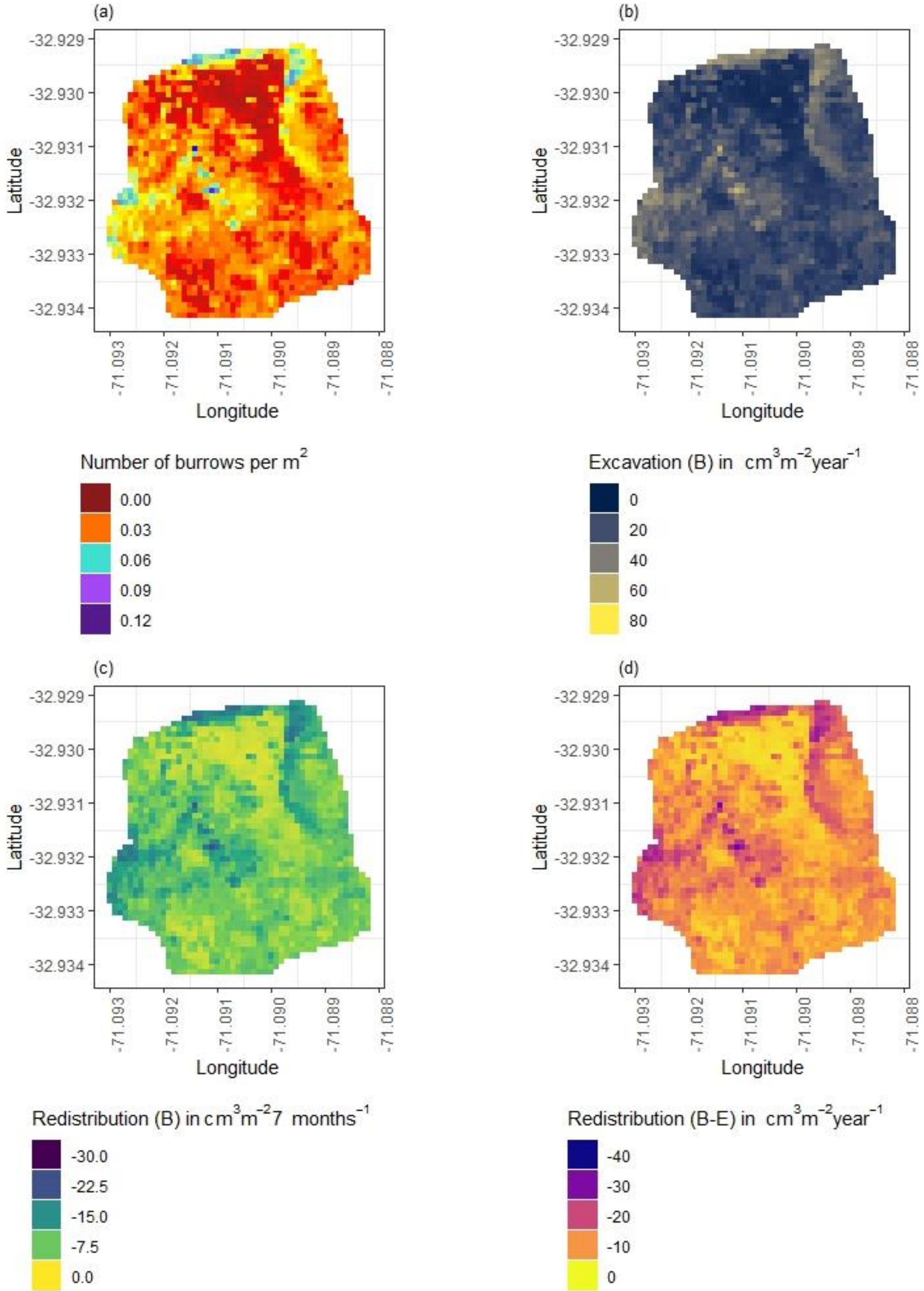

Figure 8. Example of the hillslope-wide volume of redistributed sediment on the south-facing hillslope in La Campana: (a) Density of burrows as estimated by Grigusova et al. (2021); (b) Volume of the sediment excavated by the animals; (c) Volume of the sediment redistributed during rainfall events within burrows; (d) Volume of additionally redistributed sediment during rainfall events due to the presence of the burrows. The values were calculated per burrow as stated in Section 3.7. by subtracting the sediment volume redistributed within burrows from the sediment volume redistributed within burrow embedding area and then upscaled. The letters in brackets indicate if the upscaling was conducted using data from burrows or burrow embedding areas.

"B" stands for burrow. By "EM-B", the redistribution calculated within burrow embedding areas was subtracted from the redistribution calculated within burrows to obtain the additional volume of redistributed sediment due to the burrows' presence.

5. Discussion

Our results showed that the custom-made ToF device is a suitable tool for high-resolution, automated monitoring of surface changes, applicable also in remote areas. The ability of a continuous observation of sediment redistribution over a longer time during our study provided new insights into the importance of burrowing animals for sediment redistribution. Our research reveals that the presence of vertebrate burrows increases hillslope sediment redistribution rates much more than previously assumed (up to 208%). We showed that the quantity of animal-related sediment redistribution, however, varied with rainfall occurrence, with an increase in sediment redistribution between 40% in the arid research area and 338% percent in the mediterranean research area.

5.1 Suitability of the ToF method for surface monitoring

The here proposed monitoring technique enables an automatic monitoring of surface changes on a microtopographic scale, and its measurement continuity allows for the analysis of ongoing biogeomorphological processes in high temporal resolution.

With regard to the costs, measurement frequency and sampling autonomy, the custom-made ToF device stands in contrast to earlier studies that used laser scanning technology to monitor microtopographic changes (Table A5). Previous studies mainly applied expensive laser scanning for the estimation of sediment redistribution, and the research sites had to be personally revisited for each of the measurements (Nasermoaddeli und Pasche 2008; Eltner et al. 2016a; Eltner et al. 2016b; Hänsel et al. 2016). The estimated costs in studies using time-lapse photogrammetry were similar to our study (up to 5000 USD) (James und Robson 2014; Galland et al. 2016; MALLALIEU et al. 2017; Eltner et al. 2017; Kromer et al. 2019; Blanch et al. 2021). However, for time-lapse monitoring, several devices needing different viewing angles increases installation efforts significantly.

In terms of data quality, our ToF device is more precise or comparable to those employed in other studies. The accuracy of the camera (R^2 = 0.77) was in the range of previous studies (R^2 = 0.26–0.83 (Eitel et al. 2011), Table A5). The horizontal point spacing of our cameras was 0.32 cm, and the maximum number of points per cm^2 was 8.5. These values are similar to previous studies in which the used devices had a horizontal point spacing in the range of 0.25–0.57 cm (Kaiser et al. 2014; Nasermoaddeli und Pasche 2008)) (Table A5), and the maximum number of points per cm^2 in a range of 1 point–25 points cm^{-2} (Eitel et al. 2011; Longoni et al. 2016) (Table A5).

Our cameras tended to slightly overestimate or underestimate the volume of redistributed sediment. This error occurs when the pulse reflects from several vertical objects such as walls or, in our case, branches or stones and then enters the camera sensor. This phenomenon was also observed in previous studies applying laser scanners and is inevitable if the goal is to study surface changes under natural field conditions (Kukko und Hyyppä 2009; Ashcroft et al. 2014). During operation of the cameras, we learnt that our newly developed instruments are particularly capable of delivering usable scans at night. This is likely due to the strong scattered sunlight reaching the camera sensor during the day, blurring the data (Li 2014). Thus, in future studies, we recommend focusing on nocturnal operation to prevent light contamination from the surroundings.

We could thus prove that ToF cameras are a suitable and cost-effective method for a continuous monitoring of sediment redistribution at a microtopographic scale without the need of time, labour and cost intensive laser scanning/time-lapse photogrammetry campaigns.

5.2 Burrowing cycles and climate variability

Our monitoring covered a time period from March 2019 until October 2019. To use our temporally limited data on an annual basis, it is important to consider the annual course of burrowing. The burrowing activity of the animals varies between the families. The most common burrowing families within our study area are Canidae, Cricetidae and Octogontidae (Tab 1). Highest burrowing activity of the family Canidae was observed during breeding time between August until October (Monteverde und Piudo 2011). The peak of the burrowing activity of the family Cricetidae is in austral winter from June to August (Vargas Cademartori 2003). The burrowing activity of the rodents of the family Octogontidae depends largely on the habitat productivity. They tend to be most active from March to July (Malizia 1998). The time span, in which the most common burrowing families within our study area are active, March until October, was fully covered by our dataset. We therefore didn’t miss any burrowing activity within the current year.

Our monitoring period lasts from March until October. In 2019, March and April were dry season; May until August were rain season; and September i again dry season. Our monitoring time period is thus approximately evenly covered by dry and rain season. Furthermore, the annual variability and the variability within our monitoring time period are similar. In LC, the variance in year 2019 was 3.2 mm with a standard deviation (SD) of 1.8 mm. The variance between March 2019 and October 2019 (e.g. our monitored time period) was 3.3 mm and the SD was as well 1.8 mm. The annual variance in PdA was 0.3 mm with an SD of 0.5 mm. The variance between March 2019 and October 2019 was 0.1 mm and the SD was as well 0.4 mm. We can therefore upscale our values to the time period of one year.

As for the precipitation, in the years 2017, 2018 and 2019, strong inter-annual climate variability and strongly declining precipitation rate was detected. In LC, the precipitation amounted 351 mm in 2017, 245 mm in 2018 and 72 mm in 2019. The inter – annual variance was 16.5 mm with an SD of 4.1 mm. In PdA, the precipitation amounted 16.2 mm in 2017, 8 mm in 2018 and 15 mm in 2019. The inter – annual variance was 0.2 mm with an SD of 0.4 mm. Compared with previous years, our results might on average underestimate rainfall-induced erosion rates. However, the relative erosion rate compared between burrow area and burrow embedding area would stay the same.

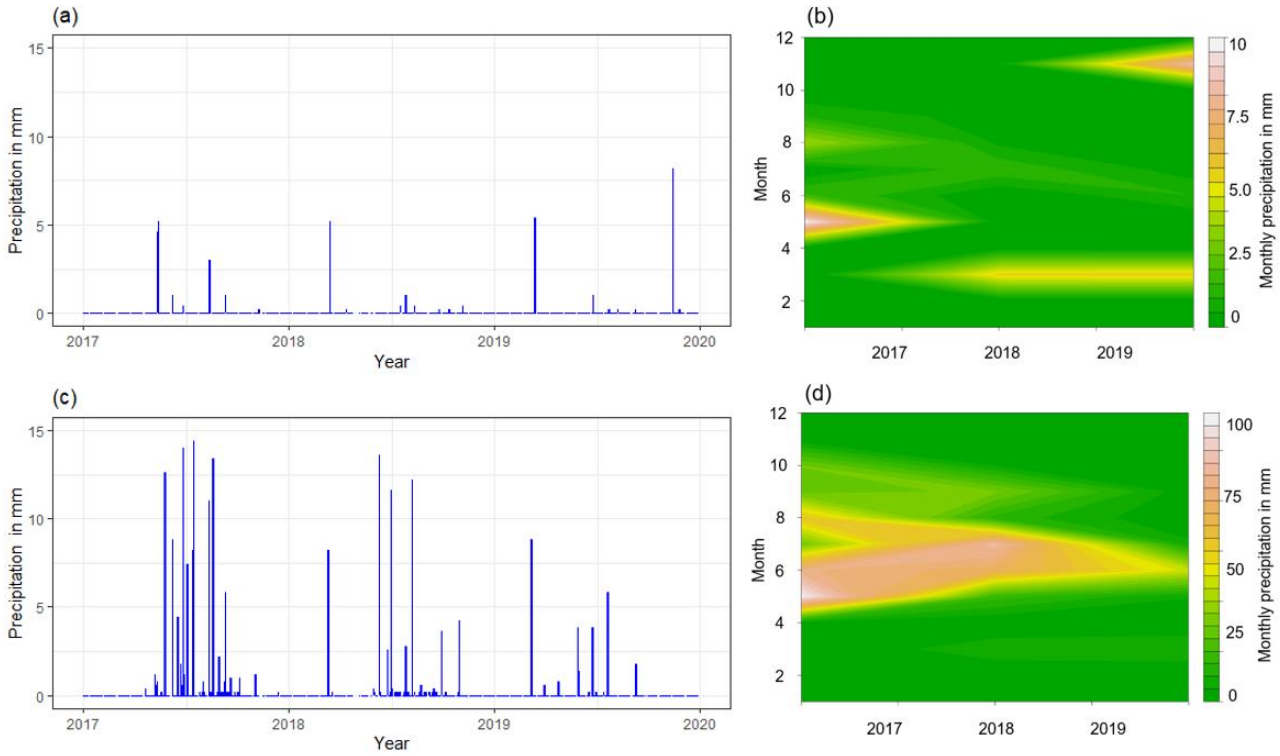

Figure 9. Climate variability. (a) Daily precipitation in PdA. (b) Monthly precipitation in PdA. (c) Daily precipitation in LC. (d) Monthly precipitation in LC.

5.3. Sediment Redistribution

Our research reveals that the presence of vertebrate burrows generally increases hillslope sediment redistribution. We show, however, that the ratio between the sediment redistribution caused by rainfall within burrow and burrow embedding areas varies between climate zones. Sediment redistribution within burrow areas was 40% higher at the arid research site, and at the mediterranean research site, it was 338% higher when compared to burrow embedding area (Table A6).

By monitoring microtopographical changes in a high spatio-temporal resolution, we found that the occurrence of larger rainfall events played a two-fold, accelerating role in influencing sediment redistribution (Fig. 10). Firstly, rainfall-runoff eroded burrow material caused increased sediment loss. This was followed by animal burrowing activity after the rainfall. This means that rainfall triggered animal burrowing activity which was very likely related to a lower burrowing resistance of the soil due to the increased soil moisture (Rutin 1996; Romañach et al. 2005; Herbst und Bennett 2006). This double feedback led to frequently occurring but small redistribution rates. However, cumulatively, the mechanism increased downhill sediment fluxes. Previous studies most likely missed this low magnitude but frequent surface processes due to a lower monitoring duration and frequency, or artificial laboratory conditions, and thus, did not quantify the full volume of redistributed sediment associated with burrowing activity. To quantify all occurred sediment redistribution processes, a continuous surface monitoring, like the here presented, is needed.

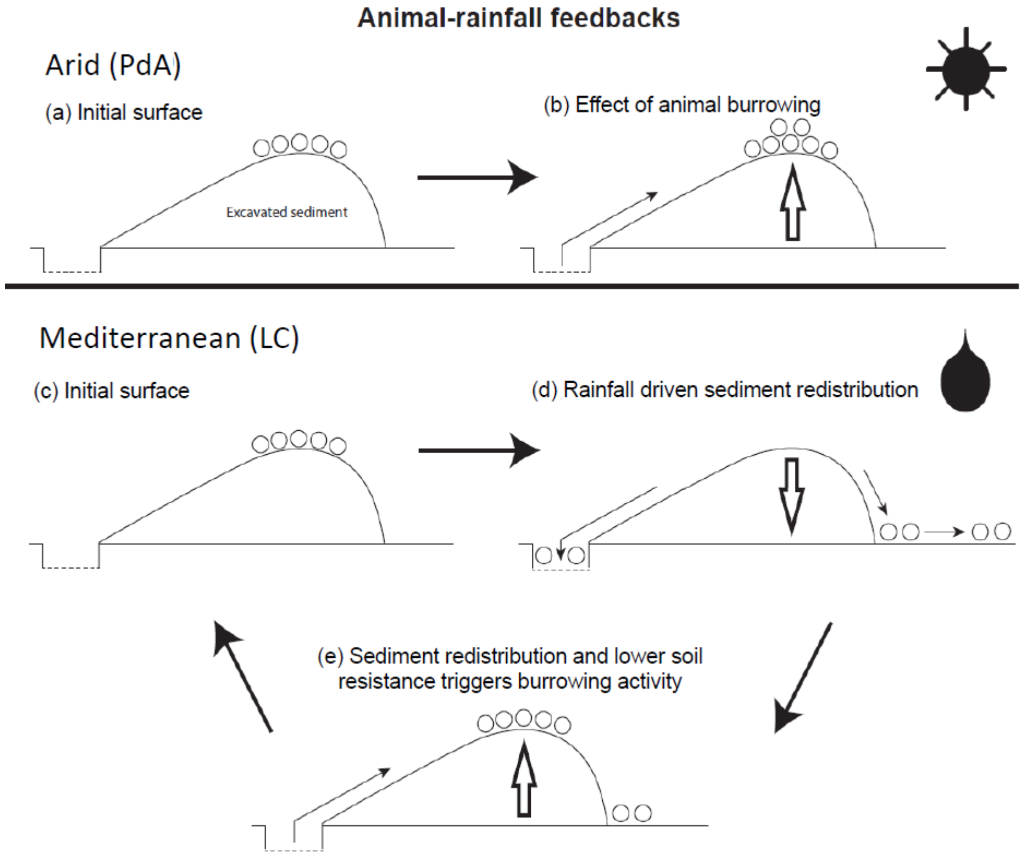

Figure 10. Scheme of animal-driven and rainfall-driven sediment redistribution processes in both investigated climate zones: (**a**) Describes the initial surface of the burrow before the start of a sediment redistribution process, and (**b**) the animal excavation process in the arid climate zone. Here, due to rarely occurring rainfall events, sediment redistribution is mostly controlled by the animal burrowing activity; (**c**) describes the initial burrow surface in the mediterranean climate zone, (**d**) the process of sediment redistribution during a rainfall event and (**e**) the subsequent animal burrowing activity. Burrowing is triggered by decreased soil resistance due to the increased soil moisture after rainfall as well as by sediment accumulation within the burrow's entrance. Burrowing activity leads to a new supply of sediment being excavated to the surface. In the mediterranean climate zone, sediment redistribution is controlled by both animal burrowing activity and rainfall. The alternating excavation and erosion process ultimately lead to an increase in redistribution rates.

Our results indicate an up to 338% increase in the sediment volume redistributed during rainfall events measured within burrows when compared to burrow embedding areas. In contrast to our result, the maximum increase estimated in previous studies was 208% (Table A6, (Imeson und Kwaad 1976). The two climate zones also show different patterns: In the mediterranean climate, the contribution of animals' (vertebrates') burrowing activity appear larger than previously observed by using field methods such as erosion pins or splash traps (from –3% until – 208%, Table A6, (Imeson und Kwaad 1976; Hazelhoff et al. 1981; Black und Montgomery 1991). In contrast, in arid PdA, our study found a much smaller increase (40%, Table A6) in the sediment volume redistributed during rainfall events measured within burrows when compared to burrow embedding areas. This is lower than previously estimated (125%, Table A6, (Black und Montgomery 1991). However, solely one rainfall event above 0.2 mm day^{-1} occurred during our monitoring period. Hence, we conclude that the contribution of burrowing activity of animals to hillslope sediment transport is much larger in areas with frequent rainfall events than previously thought, while it has been realistically estimated by previous studies for areas with rare rainfall events (Table A6).

Magnitudes of sediment volume redistributed within burrows similar to our results were previously obtained solely in studies applying rainfall simulators. These studies estimated an increase in the volume of sediment redistributed during rainfall events, measured within burrows when compared to burrow embedding areas, to be between 205% and 473% (Table A6, (Li et al. 2018; Chen et al. 2021). However, a rainfall simulator can only provide data on surface processes within a plot of a few m^2 in size and under ideal laboratory conditions while ignoring the uphill microtopography, vegetation cover and distribution (Iserloh et al. 2013), which were shown to reduce erosion rates. More importantly, the rainfall intensity on hillslopes decreases with (i) the angle of incidence of the rain, (ii) the inclination of the surface and iii) the relative orientation of the sloping surface to the rain vector (Sharon 1980). When simulating a rainfall event with the same rainfall volume as in the field, the rain is induced directly over the treated surface and has thus a higher velocity which leads to an increased splash erosion than under natural conditions (Iserloh et al. 2013). We thus propose that the rainfall experiments overestimate the erosion rate while the correct erosion rate can be measured solely under field conditions.

Cumulative sediment redistribution within burrow roof, mound and entrance was, on average, 28% lower than cumulative sediment redistribution only within the mound and the burrow roof (Figure A7). These results suggest that 28% of the eroded sediment from animal mounds and burrow roofs is re-accumulated within the burrow entrance during rainfall-runoff events, and the remaining 62% is incorporated into overall hillslope sediment flux. Our numbers contrast with previous studies, which quantified that about 58% of the sediment excavated by animals will accumulate back in the burrow entrance and only 42% is incorporated to downhill sediment flux (Andersen 1987; Reichman und Seabloom 2002). Hence, our results indicate not only higher redistribution rates within burrows by burrowing animals but also point to much higher supply of sediment to the downhill sediment flux than previously thought.

Our cost-effective ToF device provides data on surface changes in a high spatio-temporal resolution. The high temporal resolution was able to unravel ongoing low magnitude but frequent animal excavation and erosion processes. The high spatial resolution enabled us to estimate the exact volume of sediment fluxes from the burrows downhill. The here presented results indicate that the contribution of burrowing animals on the burrow as well as on the hillslope scale was much higher than previously assumed. Our results can be integrated into long-term soil erosion models that rely on soil processes and improve their accuracy by including animal-induced surface processes on microtopographical scales in their algorithms.

Funding: This study was funded by the German Research Foundation, DFG [grant numbers BE1780/52-1, LA3521/1-1, FA 925/12-1, BR 1293-18-1], and is part of the DFG Priority Programme SPP 1803: EarthShape: Earth Surface Shaping by Biota, sub-project “Effects of bioturbation on rates of vertical and horizontal sediment and nutrient fluxes”.

Institutional Review Board Statement: Not applicable.

Informed Consent Statement: Not applicable.

Acknowledgments: We thank CONAF for the kind support provided during our field campaign.

Competing interests: There is no conflict of interest.

Author contribution: JB, AL and SA planned the campaign; PG and SA performed the measurements; PG analysed the data and wrote the manuscript draft; AL, JB, NF, RB, KÜ, LP, CR, DK and PP reviewed and edited the manuscript.

Code/Data availability: Code and all raw data can be provided by the corresponding author upon request.

Appendices

Table A1. List of abbreviations

α [°]	**Tilt angle of the camera**
b [°]	Surface inclination
Ω	Threshold value for the scan scattering error
B	Burrow
$Area_{burrow}$	mean in the field measured size of the burrows which are monitored
Area	total surface area monitored by the camera
BD	Bulk density
c [m/s]	Speed of light
D	Distance from the camera to the object
$Dens_{burrow}$	Burrow density
DSM	Digital surface model
DSM_{after}	DSM calculated from the scan taken after the extraction
DSM_{before}	DSM calculated from the scan taken before the extraction
EM	Burrow embedding area
Entrance	entrance to the animal burrow
g [-]	ratio [-] of the reflected photons to all photons
LC	National Park LC
LC-NL	Camera in LC on the lower north-facing hillslope
LC-NU	Camera in LC on the upper north-facing hillslope
LC-SL	Camera in LC on the lower south-facing hillslope
LC-SU	Camera in LC on the upper south-facing hillslope
MAE	Mean absolute error
MAP [°]	Mean annual precipitation
m.a.s.l.	Meters above sea level
MAT	Mean annual temperature
mClay [%]	Mean content of clay
$mean_{z\text{-}coordinate}$	Mean value of the z-coordinates
Mound	the sediment excavated by the animal while digging the burrow
mSand [%]	Mean content of sand
mSilt [%]	Mean content of silt
n	Number of scans
PdA	National Park Pan de Azúcar
PdA-NL	Camera in PdA on the lower north-facing hillslope

PdA-NU	Camera in PdA on the upper north-facing hillslope
PdA-SL	Camera in PdA on the lower south-facing hillslope
PdA-SU	Camera in PdA on the upper south-facing hillslope
Res	Resolution
Roof	sediment pushed aside and uphill the entrance during burrow creation
S_a	scan after the rainfall event
S_b	scan before the rainfall event
SBC	Single board computer
$sd_{z\text{-}coordinate}$	standard deviation of the z-coordinates
SSH	Secure shell
t [s]	Overall time of camera illumination
TOC [%]	Total organic carbon
ToF	Time-of-Flight
Vol_{burrow}	volume of redistributed sediment within burrow
$Vol_{detected}$	volume of the extracted sediment as detected by the camera
Vol_{add}	difference in redistributed sediment volume between burrows and burrow embedding areas
Vol_{exc}	Volume of the sediment excavated by the animal
$Vol_{hillslope\text{-}wide}$	Hillslope-wide volume of redistributed sediment
$Vol_{measured}$	volume of the extracted sediment measured by the measuring cup
$Vol_{per\ burrow}$	Volume of redistributed sediment per burrow
$Vol_{per\ pixel}$	Volume of redistributed sediment per pixel
$Vol_{redistributed}$	volume of the calculated redistributed sediment
$Vol_{embedding}$	volume of redistributed sediment within burrow embedding area
y_i	distance of the point to the point of origin at the camera nadir
z_{cor}	Corrected z-coordinate
z_{uncor}	Uncorrected z-coordinate

Table A2. Number of usable scans for each camera

Camera	Latitude	Longitude	Number of scans	Percentage of usable scans taken at 1am / 5am / 8am / 10pm	Time period
PdA-NU	-25.98131	-70.6166	238	29 / 27 / 20 / 24	18.3.-18.9.
PdA-NL	-25.98277	-70.61278	52	24 / 0 / 40 / 36	27.3.-31.5
PdA-SU	-25.97477	-70.61641	351	30 / 26 / 32 / 11	16.3.-19.9.
PdA-SL	-25.97177	-70.61409	167	48 / 38 / 7 / 8	16.3.-19.9.
LC-NU	-32.95230	-71.06231	215	37 / 20 / 8 / 33	9.3.-9.9.
LC-NL	-32.93928	-71.08613	3	-	6.3.-12.9
LC-SU	-32.93078	-71.09066	160	22 / 28 / 26 / 25	28.3.-22.5
LC-SL	-32.93110	-71.08987	167	27 / 25 / 22 / 26	16.3.-19.9.

Table A3. Summary of the volume of redistributed sediment, according to area and disturbance type. Vol$_{exc}$ describes volume of the sediment excavated by the animals. Vol$_{burrow}$ describes volume of the sediment redistributed during rainfall events within burrows. Vol$_{add}$ describes the difference in redistributed sediment volume within burrows and burrow embedding area during rainfall.

Disturbance	**Area**	**PdA**	**LC**
Vol$_{exc}$	Burrow	16.41 cm^3 cm^{-2} year^{-1}	14.62 cm^3 cm^{-2} year^{-1}
	Per burrow	1498.66 cm^3 burrow^{-1} year^{-1}	1226.61 cm^3 burrow^{-1} year^{-1}
	Hillslope-wide	0.18 m^3 ha^{-1} year^{-1}	0.67 m^3 ha^{-1} year^{-1}
Vol$_{burrow}$	Burrow	-1.97 cm^3 cm^{-2} year^{-1}	-10.44 cm^3 cm^{-2} year^{-1}
	Per burrow	-126.36 cm^3 burrow^{-1} year^{-1}	-876.38 cm^3 burrow^{-1} year^{-1}
	Hillslope-wide	-0.05 m^3 ha^{-1} year^{-1}	-0.48 m^3 ha^{-1} year^{-1}
Vol$_{add}$	Burrow	-1.18 cm^3 cm $^{-2}$ year^{-1}	-7.37 cm^3 cm^{-2} year^{-1}
	Per burrow	-48.36 cm^3 burrow^{-1} year^{-1}	-619.2 cm^3 burrow^{-1} year^{-1}
	Hillslope-wide	-0.02 m^3 ha^{-1} year^{-1}	-0.34 m^3 ha^{-1} year^{-1}

Table A4. Summary of the volume of redistributed sediment, according to area and disturbance type. Vol$_{exc}$ describes volume of the sediment excavated by the animals. Vol$_{burrow}$ describes volume of the sediment redistributed during rainfall events within burrows. Vol$_{add}$ describes the difference in redistributed sediment volume within burrows and burrow embedding areas during rainfall.

Disturbance	**Area**	**PdA**	**LC**
Vol$_{exc}$	Burrow	9.57 cm^3 cm^{-2} 7 months^{-1}	8.53 cm^3 cm^{-2} 7 months^{-1}
	Per burrow	874.22 cm^3 burrow^{-1} 7 months^{-1}	715.52 cm^3 burrow^{-1} 7 months^{-1}
	Hillslope-wide	0.11 m^3 ha^{-1} 7 months^{-1}	0.39 m^3 ha^{-1} 7 months^{-1}
Vol$_{burrow}$	Burrow	-1.15 cm^3 cm^{-2} 7 months^{-1}	-6.09 cm^3 cm^{-2} 7 months^{-1}
	Per burrow	-73.71 cm^3 burrow^{-1} 7 months^{-1}	-511.22 cm^3 burrow^{-1} 7 months^{-1}
	Hillslope-wide	-0.03 m^3 ha^{-1} 7 months^{-1}	-0.28 m^3 ha^{-1} 7 months^{-1}
Vol$_{add}$	Burrow	-0.69 cm^3 cm $^{-2}$ 7 months^{-1}	-4.30 cm^3 cm^{-2} 7 months^{-1}
	Per burrow	-28.21 cm^3 burrow^{-1} 7 months^{-1}	-361.20 cm^3 burrow^{-1} 7 months^{-1}
	Hillslope-wide	-0.01 m^3 ha^{-1} 7 months^{-1}	-0.2 m^3 ha^{-1} 7 months^{-1}

Table A5. Review of studies which used laser scanners for the estimation of surface processes.

Reference	**R^2**	**Error**	**Horizontal point spacing**	**Points per cm^{-2}**	**Model**	**Price**

Our results	0.77	0.15 cm	0.32 cm	8.5	Texas Instruments OPT3101	900 USD
(Eitel et al. 2011)	0.23-0.86	0.07 cm	NA	25	Leica ScanStation 2	102 375 USD
(Eltner et al. 2013)	NA	0.4 cm	NA	6.4	Riegl LMS-Z420i	16 795 USD
(Kaiser et al. 2014)	NA	NA	0.57 cm	NA	Riegl LMS-Z420i	16 795 USD
(Longoni et al. 2016)	NA	NA	NA	1	Riegl LMS-Z420i	16 795 USD
(Morris et al. 2011)	NA	0.5 cm	NA	NA	Maptek I-Site 4400LR	240 000 USD
(Nasermoaddeli und Pasche 2008)	NA	0.2 cm	0.25 cm	NA	Leica Cyrax HDS 2500	4500 USD
(Thomsen et al. 2015)	NA	NA	0.4 cm	NA	Leica ScanStation 2	102 375 USD

Table A6. Review of studies which estimated the sediment redistribution within burrows and burrow embedding areas and the proposed impact.

Reference	**Climate**	**Animals**	**Method**	**Monitoring period**	**Frequency**	**Burrows**	**Burrow embedding area**	**impact**
(Imeson und Kwaad 1976)	continental	rodents	erosion pins	15 months	monthly	20 mm		NA
(Imeson und Kwaad 1976)	continental	rodents	splash boards	15 months	monthly	91.75g 24.49 cm^{-2} = 3.75 cm^3 cm^{-2}	94g	-3%
(Imeson und Kwaad 1976)	continental	rodents	rainfall simulation (7.5 cm / hour intensity)	One-time measurement	NA	0.2 g – 0.73 g	0.009 g – 0.23 g	+208 %
(Imeson 1977)	continental	vertebrates	rainfall simulation	One-time measurement	NA	0.18-0.3 100 J^{-1} m^{-2} rain	0.146 100 J^{-1} m^{-2} rain	+123 %

(Hazelhoff et al. 1981)	continental	earthworms	splash traps	12 months	monthly	NA	NA	+180 %
(Black und Montgomery 1991)	arid	pocket gopher	erosion pins	10 months	2 months	NA	NA	+125 %
(Hakonson 1999)	temperate	pocket gophers	rainfall simulator (60 mm / hour)	2 years	2 – 3 weeks	2.4 – 8.7 mg ha^{-1}	4.4 – 15 mg ha^{-1}	-43%
(Li et al. 2018)	temperate	mole crickets	rainfall simulation (36 mm / hour)	One time measurement	15 measurements	22.1 g 115 cm^{-2} = 5.2 cm^{3} cm^{-2}	5 g 123 cm^{-2} = 1.09 cm^{3} cm^{-2}	+473 %
(Li et al. 2018)	temperate	mole crickets	rainfall simulation (36 mm / hour)	One time measurement	15 measurements	35.3 g 220.5 cm^{-2} = 6.24 cm^{3} cm^{-2}	5 g 123 cm^{-2} = 1.09 cm^{3} cm^{-2}	+473 %
(Chen et al. 2021)	lab	chinese zocor	rainfall simulation (80 mm / hour)	One-time measurement	3 measurements	2,69 g cm^{-2} = 2.69 cm^{3} cm^{-2}	0,88 g cm^{-2} = 0.88 cm^{3} cm^{-2}	+205 %

Table A7. Review of studies which estimated the sediment redistribution within burrows, average burrow density as found in the literature and area-wide yearly contribution of burrowing animals to sediment redistribution.

Climate	**Animals**	**Burrows**	**Average burrow density**	**Average burrow size**	**Area-wide redistribution**
Continental	rodents	91.75g 24.49 cm^{-2} = 3.75 cm^{3} cm^{-2} (Imeson und Kwaad 1976)	14 625 m^{-2} = 0.02 m^{-2} (Pang und Guo 2017)	24.49 cm^{2} (Imeson und Kwaad 1976)	0.183 m^{3} ha^{-1} year^{-1}
Temperate	mole crickets	22.1 g 115 cm^{-2} = 5.2 cm^{3} cm^{-2} (Li et al. 2018)	405 ha^{-1} (Castner und Fowler 1984)	115 cm^{2} (Li et al. 2018)	0.24 m^{3} ha^{-1} year^{-1}

Temperate	mole crickets	35.3 g 220.5 cm^{-2} = 6.24 cm^3 cm^{-2} (Li et al. 2018)	405 ha^{-1} (Castner und Fowler 1984)	220.5 cm^2 (Li et al. 2018)	0.56 m^3 ha^{-1} $year^{-1}$
Lab	chinese zocor	2,69 g cm^{-2} = 2.69 cm^3 cm^{-2} (Chen et al. 2021)	94.69 2500m^{-2} = 0.04 m^{-2} = 400 ha^{-1}	1256 cm^2	1.35 m^3 ha^{-1} $year^{-1}$

Table A8. Review of studies which estimated the volume of sediment excavated by burrowing animals.

	Climate	Animals	Method	Monitoring period	Frequency	volume of the excavated sediment
(Black und Montgomery 1991)	arid	porcupines	mound volume	3 years	yearly	0.2 m^3 ha^{-1} $year^{-1}$
(Black und Montgomery 1991)	arid	isopods	mound volume	3 years	yearly	0.11 m^3 ha^{-1} $year^{-1}$
(Black und Montgomery 1991)	arid	pocket gopher	mound volume	2 years	3 model runs	0.05 – 0.11 m^3 ha^{-1} $year^{-1}$
(Rutin 1996)	subtropical	scorpions	mound volume	6 months	2-29 days	0.42 m^3 ha^{-1} $year^{-1}$
(Hall et al. 1999)	alpine	rodents	mound volume	1 year	yearly	0.02 m^3 ha^{-1} $year^{-1}$
(Hall et al. 1999)	alpine	bears	mound volume	1 year	yearly	0.49 m^3 ha^{-1} $year^{-1}$
(Yoo et al. 2005)	arid	pocket gopher	mound volume	1 year	One model run	0.1-0.2 m^3 ha^{-1} $year^{-1}$

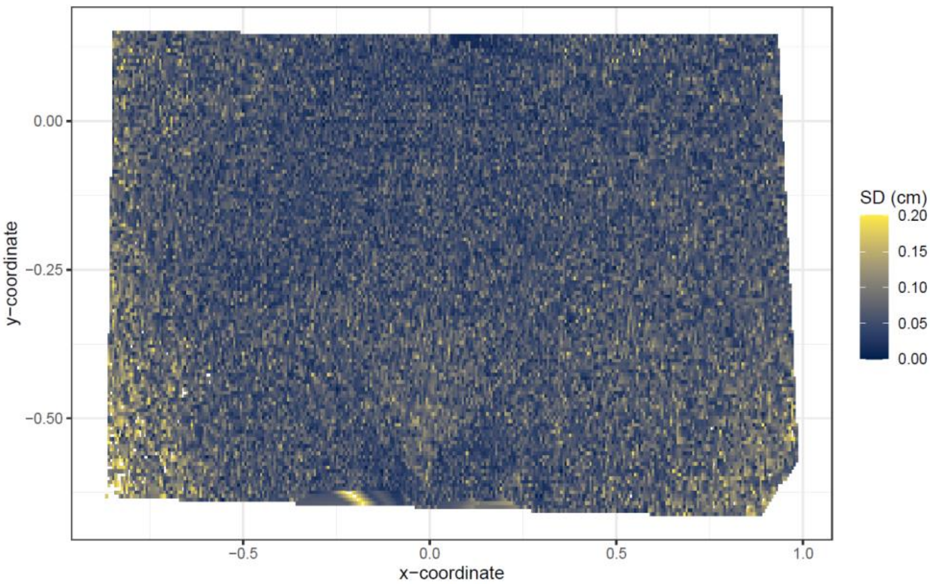

Figure A1. Standard deviation of the z-coordinate of unprocessed five scans showed exemplary for the camera on the upper north-facing hillside. SD is standard deviation. The error increases with distance from the camera nadir point. The standard deviation was here calculated from scans before any corrections.

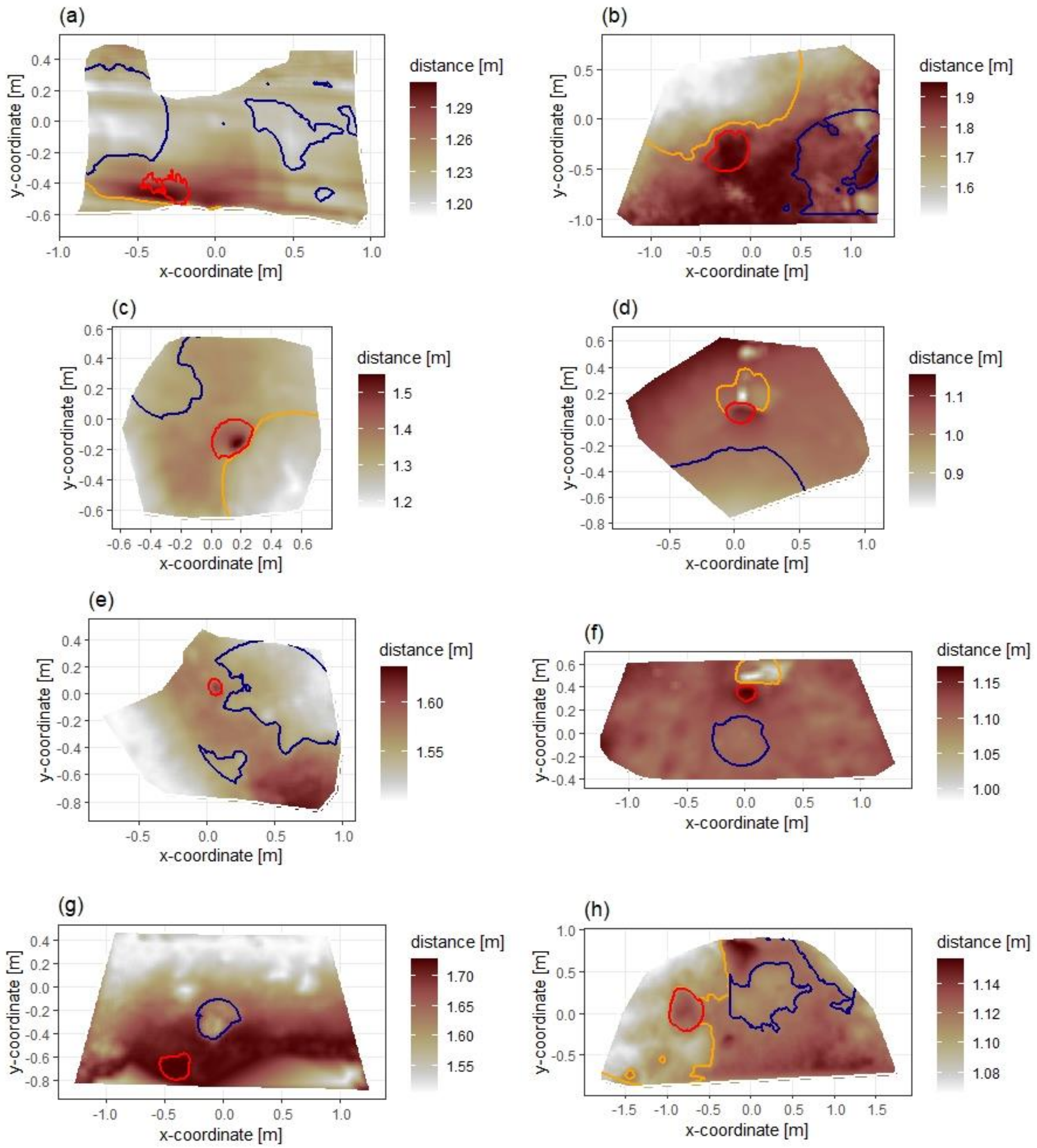

Figure A2. Delineation of the areas. The point of origin of the coordinate system is at the camera nadir. Depth is the distance between the surface and the camera. Red is the outline of the burrow entrance. Green is the outline of mound. Orange is the outline of burrow roof. Area which is not outlined is burrow embedding area. Arrow indicates downhill direction of the hillslope. (a) LC-NU. (b) LC-NL (c) LC-SU. (d) LC-SL. (e) PdA-NU. (f) PdA-NL. (g) PdA-SU. (h) PdA-SL.

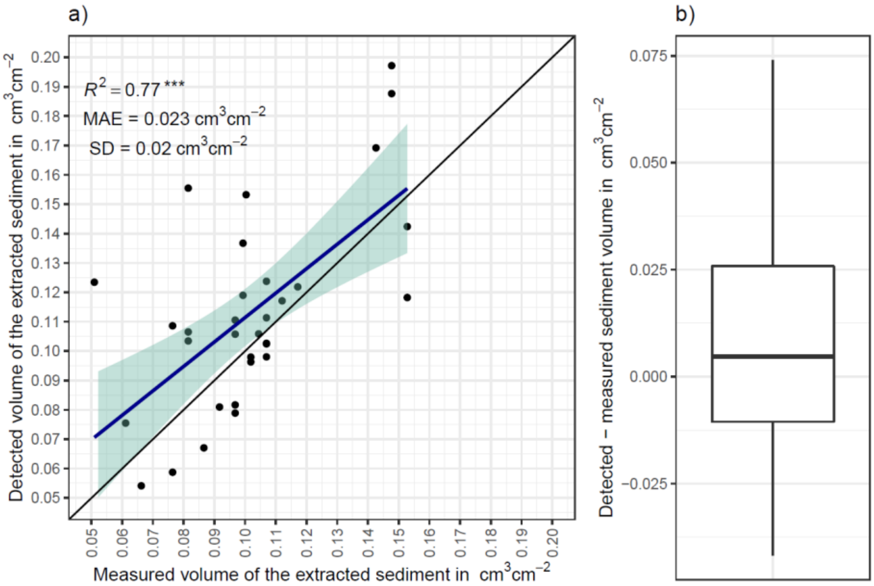

Figure A3. a) Estimation of Time-of-Flight camera accuracy based on averaging two surface scans before and after the sediment extraction under controlled conditions. The *x*-axis shows the exact sediment volume measured with a cup. The *y*-axis represents the volume of the sediment calculated from the camera scans (according to Equation (4)). The blue line is the linear regression calculated from the measured and detected volume. The green shadow shows the confidence interval of 95% for the linear regression slope. ***$p \leq 0.001$. MAE is the mean absolute error, SD is standard deviation and R^2 the coefficient of determination. b) Measured sediment volume subtracted from the detected sediment volume for all measurements.

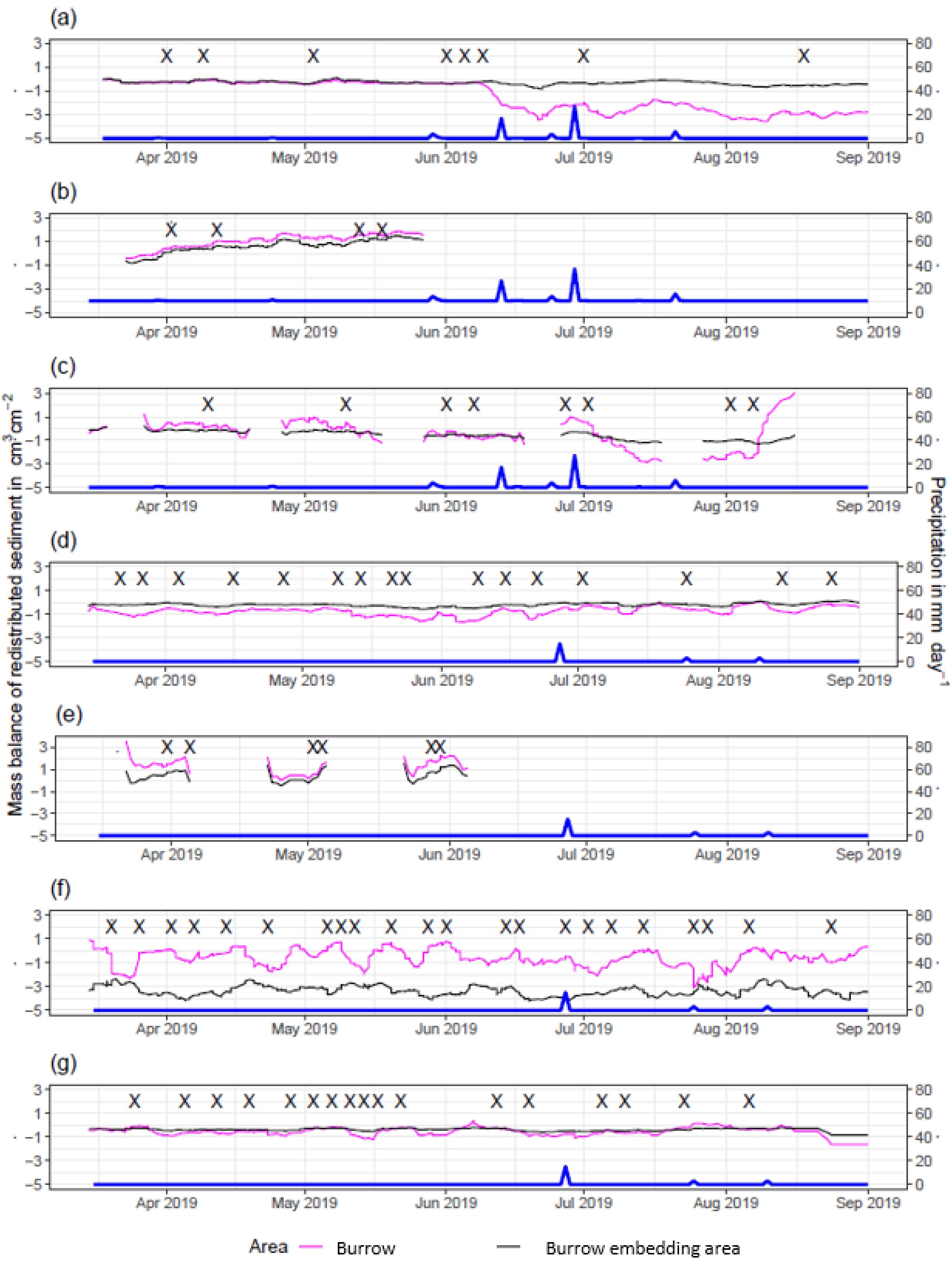

Figure A4. Sediment mass balance for the period of 7 months separately for burrows and burrow embedding areas as measured by the cameras. (a) LC-NU. (b) LC-SU. (c) LC-SL. (d) PdA-NU. (e) PdA-NL. (f) PdA-SU. (g) PdA-SL. For abbreviations see Table A1.

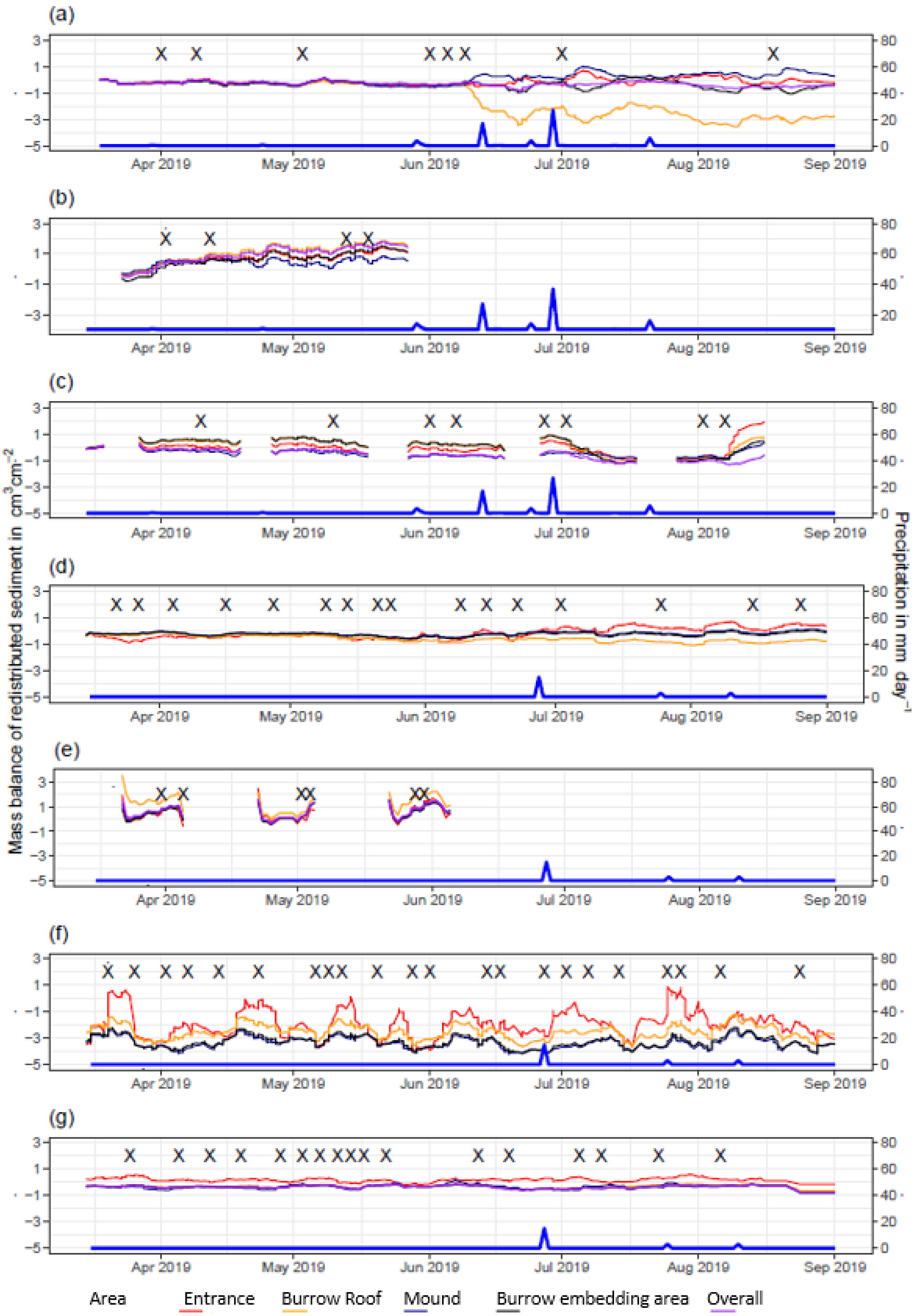

Figure A5. Sediment mass balance for the period of 7 months separately for all delineated areas as measured by the cameras. (a) LC-NU. (b) LC-SU. (c) LC-SL. (d) PdA-NU. (e) PdA-NL. (f) PdA-SU. (g) PdA-SL. For abbreviations see Table A1.

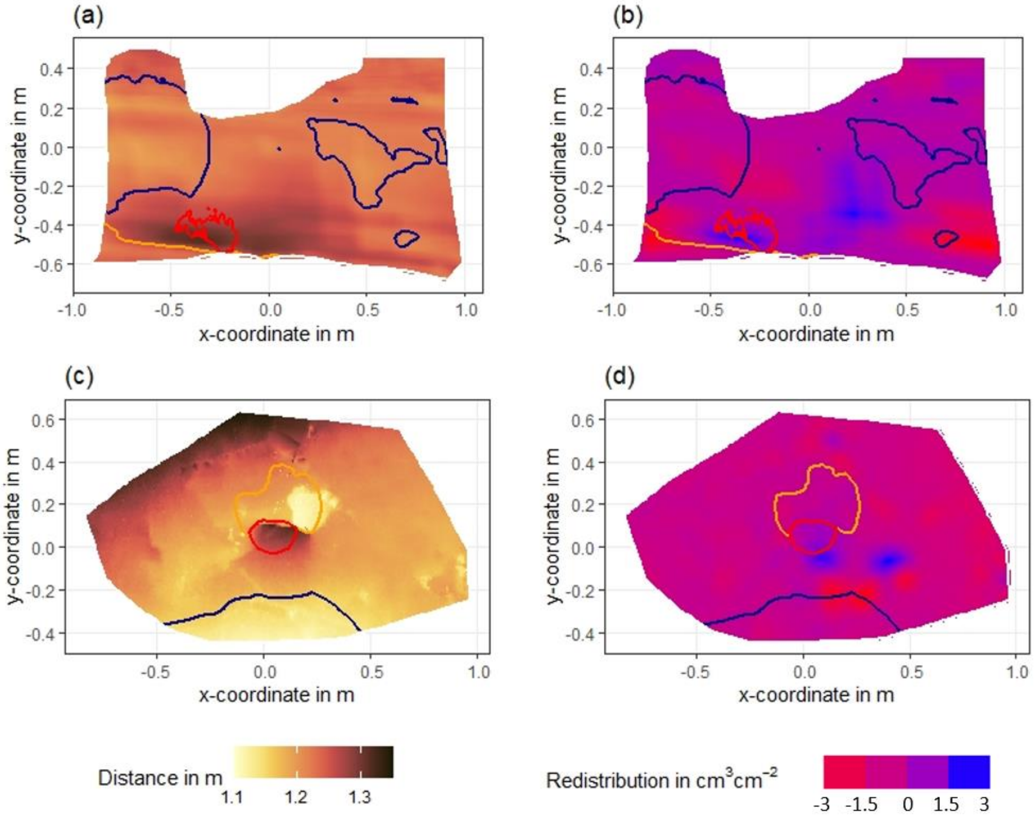

Figure A6. Examples of surface scans showing the digital surface model (DSM) before a rainfall event (**a**, **c**) at two camera locations in La Campana, and the calculated volume of redistributed sediment (**b**, **d**) after the rainfall event: (**a**) DSM of a scan from the camera on the upper north-facing hillslope in La Campana; (**b**) Detected sediment redistribution (cm^3 cm^{-2}) on the upper north-facing hillslope in La Campana after a rainfall event of 17.2 mm day^{-1}; (**c**) DSM of a scan from the camera on the upper south-facing hillslope in La Campana; (**d**) Detected sediment redistribution (cm^3 cm^{-2}) on the upper south-facing hillslope after a rainfall event of 17.2 mm day^{-1}. Red is the outline of the burrow entrance. Green is the outline of mound. Orange is the outline of the burrow roof. The area which is not outlined is burrow embedding area. Redistribution is the volume of the redistributed sediment, either accumulated (positive value) or eroded (negative value) per cm^3 cm^{-2}. After the rainfall events, sediment mostly accumulated within the burrow entrance or near mounds and eroded from burrow roofs and mounds.

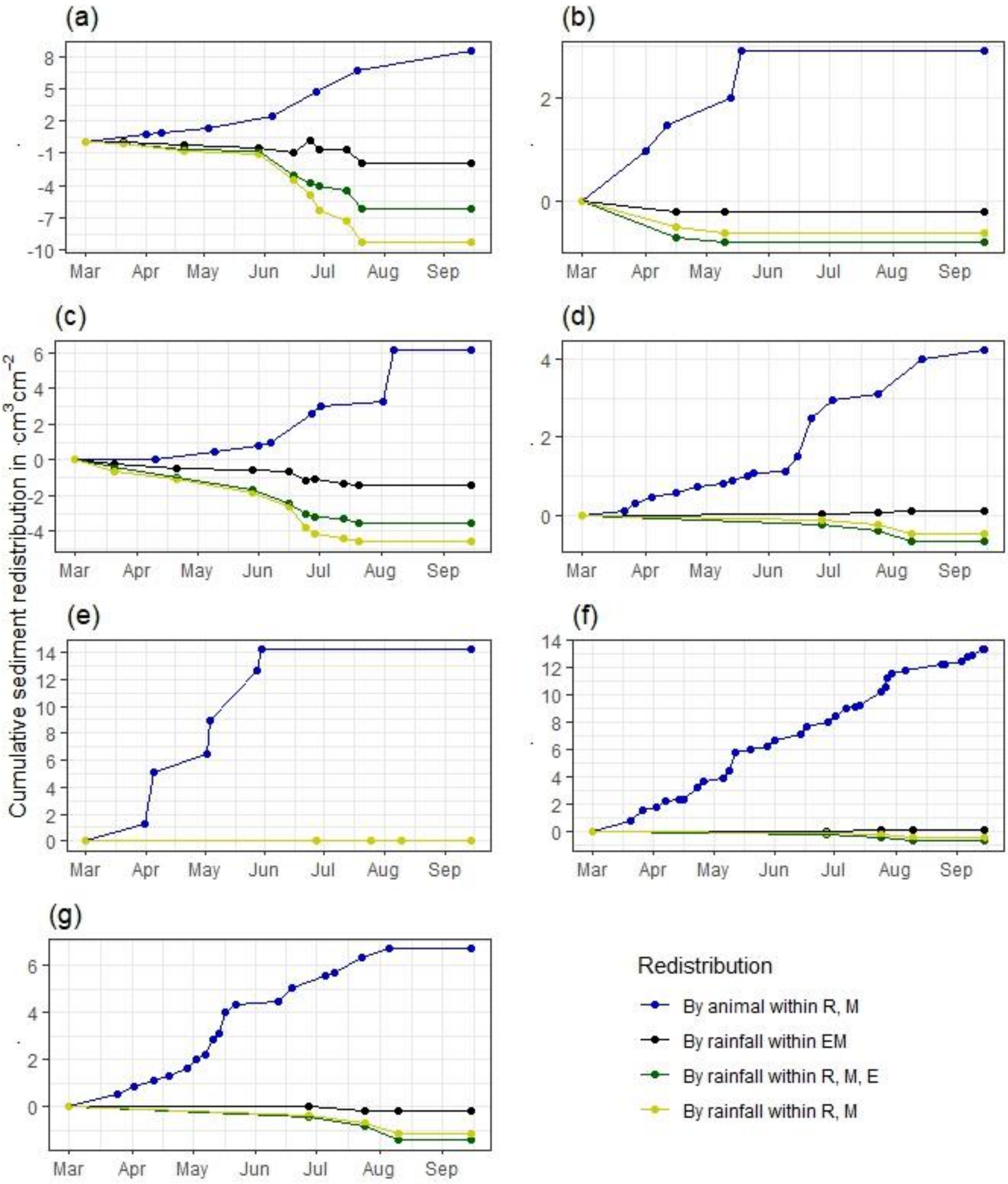

Figure A7. Cumulative volume of redistributed sediment for all cameras. Positive values indicate sediment accumulation. Negative values indicate sediment erosion. Whiskers are the median sediment redistribution. E is the burrow entrance. M is the mound. R is burrow roof. EM is burrow embedding area. LC is mediterranean climate zone. PdA is arid climate zone. (a) LC-NU. (b) LC-SU. (c) LC-SL. (d) PdA-NU. (e) PdA-NL. (f) PdA-SU. (g) PdA-SL. For abbreviations see Table A1.

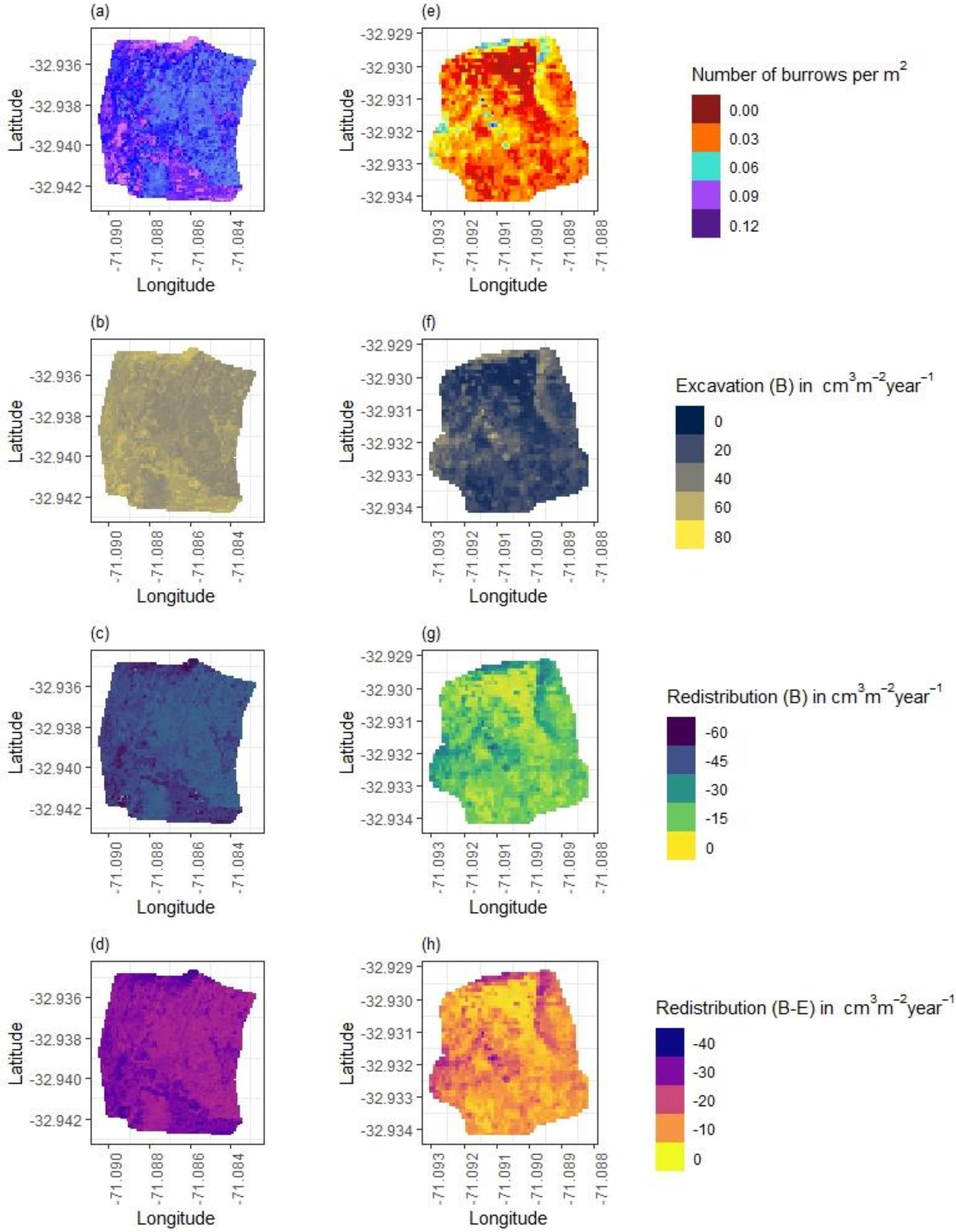

Figure A8. Hillslope-wide volume of redistributed sediment for a time period of one year in LC. (a-d) North-facing hillslope. (e-h) South-facing hillslope. (a) and (e) Density of burrows as estimated by Grigusova et al. 2021. (b) and (f) Volume of the sediment excavated by the animals. (c) and (g) Volume of the sediment redistributed during rainfall events within burrows. (d) and (h) Volume of additionally redistributed sediment during rainfall events due to presence of the burrows. The values were calculated per burrow as stated in section 3.7 by subtracting the sediment volume redistributed within burrows from the sediment volume redistributed within burrow embedding area and then upscaled. B stays for burrow, EM stays for burrow embedding area.

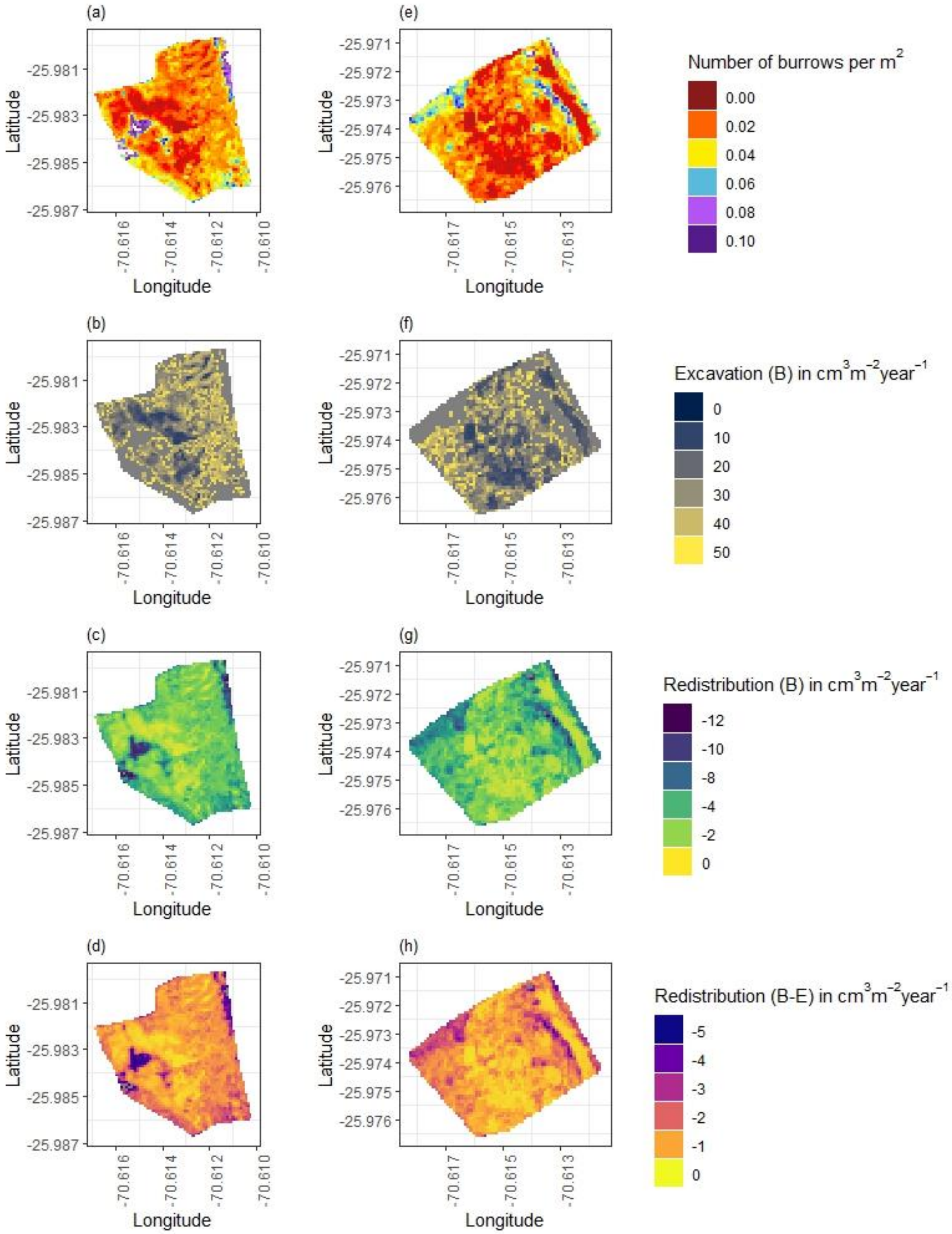

Figure A9. Hillslope-wide volume of redistributed sediment for a time period of one year in Pan de Azúcar. (a-d) North-facing hillslope. (e-h) South-facing hillslope. (a) and (e) Density of burrows as estimated by Grigusova et al. 2021. (b) and (f) Volume of the sediment excavated by the animals. (c) and (g) Volume of the sediment redistributed during rainfall events within burrows. (d) and (h) Volume of additionally redistributed sediment during rainfall events due to presence of the burrows. The values were calculated per burrow as stated in section 3.7 by subtracting the sediment volume redistributed within burrow from the sediment volume redistributed within burrow embedding area and then upscaled. B stays for burrow, EM stays for burrow embedding area by the burrowing animal.

Literaturverzeichnis

Afana, A.; Solé-Benet, A.; Pérez, J. L. (2010): Determination of Soil Erosion Using Laser Scanners. Experimental Station of Arid Zone, CSIC, Almeria, Spain, zuletzt geprüft am 22.12.2021.

Andersen, Douglas C. (1987): Geomys Bursarius Burrowing Patterns: Influence of Season and Food Patch Structure. In: *Ecology* 68 (5), S. 1306–1318. DOI: 10.2307/1939215.

Ashcroft, Michael B.; Gollan, John R.; Ramp, Daniel (2014): Creating vegetation density profiles for a diverse range of ecological habitats using terrestrial laser scanning. In: *Methods Ecol Evol* 5 (3), S. 263–272. DOI: 10.1111/2041-210X.12157.

BANCROFT, W. J.; HILL, D.; ROBERTS, J. D. (2004): A new method for calculating volume of excavated burrows: the geomorphic impact of Wedge-Tailed Shearwater burrows on Rottnest Island. In: *Funct Ecology* 18 (5), S. 752–759. DOI: 10.1111/j.0269-8463.2004.00898.x.

Bernhard, Nadine; Moskwa, Lisa-Marie; Schmidt, Karsten; Oeser, Ralf A.; Aburto, Felipe; Bader, Maaike Y. et al. (2018): Pedogenic and microbial interrelations to regional climate and local topography: New insights from a climate gradient (arid to humid) along the Coastal Cordillera of Chile. In: *CATENA* 170 (4), S. 335–355. DOI: 10.1016/j.catena.2018.06.018.

Black, Thomas A.; Montgomery, David R. (1991): Sediment transport by burrowing mammals, Marin County, California. In: *Earth Surf. Process. Landforms* 16 (2), S. 163–172. DOI: 10.1002/esp.3290160207.

Blanch, Xabier; Eltner, Anette; Guinau, Marta; Abellan, Antonio (2021): Multi-Epoch and Multi-Imagery (MEMI) Photogrammetric Workflow for Enhanced Change Detection Using Time-Lapse Cameras. In: *Remote Sensing* 13 (8), S. 1460. DOI: 10.3390/rs13081460.

Castner, James L.; Fowler, H. G. (1984): Distribution of Mole Crickets (Orthoptera: Gryllotalpidae: Scapteriscus) and the Mole Cricket Parasitoid Larra bicolor (Hymenoptera: Sphecidae) in Puerto Rico. In: *The Florida Entomologist* 67 (3), S. 481. DOI: 10.2307/3494730.

Chen, Mingyu; Ma, Li; Shao, Ming'an; Wei, Xiaorong; Jia, Yuhua; Sun, Shuchen et al. (2021): Chinese zokor (Myospalax fontanierii) excavating activities lessen runoff but facilitate soil erosion – A simulation experiment. In: *CATENA* 202 (8), S. 105248. DOI: 10.1016/j.catena.2021.105248.

Coombes, Martin A. (2016): Biogeomorphology: diverse, integrative and useful. In: *Earth Surf. Process. Landforms* 41 (15), S. 2296–2300. DOI: 10.1002/esp.4055.

Corenblit, Dov; Corbara, Bruno; Steiger, Johannes (2021): Biogeomorphological eco-evolutionary feedback between life and geomorphology: a theoretical framework using fossorial mammals. In: *Die Naturwissenschaften* 108 (6), S. 55. DOI: 10.1007/s00114-021-01760-y.

Eitel, Jan U.H.; Williams, C. Jason; Vierling, Lee A.; Al-Hamdan, Osama Z.; Pierson, Frederick B. (2011): Suitability of terrestrial laser scanning for studying surface roughness effects on concentrated flow erosion processes in rangelands. In: *CATENA* 87 (3), S. 398–407. DOI: 10.1016/j.catena.2011.07.009.

Eltner, A.; Mulsow, C.; Maas, H.-G. (2013): QUANTITATIVE MEASUREMENT OF SOIL EROSION FROM TLS AND UAV DATA. In: *Int. Arch. Photogramm. Remote Sens. Spatial Inf. Sci.* XL-1/W2, S. 119–124. DOI: 10.5194/isprsarchives-XL-1-W2-119-2013.

Eltner, A.; Schneider, D.; Maas, H.-G. (2016a): INTEGRATED PROCESSING OF HIGH RESOLUTION TOPOGRAPHIC DATA FOR SOIL EROSION ASSESSMENT CONSIDERING DATA ACQUISITION SCHEMES AND SURFACE PROPERTIES. In: *Int. Arch. Photogramm. Remote Sens. Spatial Inf. Sci.* XLI-B5, S. 813–819. DOI:

10.5194/isprsarchives-XLI-B5-813-2016.
Eltner, Anette; Kaiser, Andreas; Abellan, Antonio; Schindewolf, Marcus (2017): Time lapse structure-from-motion photogrammetry for continuous geomorphic monitoring. In: *Earth Surf. Process. Landforms* 42 (14), S. 2240–2253. DOI: 10.1002/esp.4178.
Eltner, Anette; Kaiser, Andreas; Castillo, Carlos; Rock, Gilles; Neugirg, Fabian; Abellán, Antonio (2016b): Image-based surface reconstruction in geomorphometry – merits, limits and developments. In: *Earth Surf. Dynam.* 4 (2), S. 359–389. DOI: 10.5194/esurf-4-359-2016.
Gabet, Emmanuel J.; Reichman, O. J.; Seabloom, Eric W. (2003): The Effects of Bioturbation on Soil Processes and Sediment Transport. In: *Annu. Rev. Earth Planet. Sci.* 31 (1), S. 249–273. DOI: 10.1146/annurev.earth.31.100901.141314.
Galland, Olivier; Bertelsen, Håvard S.; Guldstrand, Frank; Girod, Luc; Johannessen, Rikke F.; Bjugger, Fanny et al. (2016): Application of open-source photogrammetric software MicMac for monitoring surface deformation in laboratory models. In: *J. Geophys. Res. Solid Earth* 121 (4), S. 2852–2872. DOI: 10.1002/2015JB012564.
Grigusova, Paulina; Larsen, Annegret; Achilles, Sebastian; Klug, Alexander; Fischer, Robin; Kraus, Diana et al. (2021): Area-Wide Prediction of Vertebrate and Invertebrate Hole Density and Depth across a Climate Gradient in Chile Based on UAV and Machine Learning. In: *Drones* 5 (3), S. 86. DOI: 10.3390/drones5030086.
Hakonson, T. E. (1999): The Effects of Pocket Gopher Burrowing on Water Balance and Erosion from Landfill Covers. In: *J. environ. qual.* 28 (2), S. 659–665. DOI: 10.2134/jeq1999.00472425002800020033x.
Hall, Kevin; Boelhouwers, Jan; Driscoll, Kevin (1999): Animals as Erosion Agents in the Alpine Zone: Some Data and Observations from Canada, Lesotho, and Tibet. In: *Arctic, Antarctic, and Alpine Research* 31 (4), S. 436–446. DOI: 10.1080/15230430.1999.12003328.
Hancock, Greg; Lowry, John (2021): Quantifying the influence of rainfall, vegetation and animals on soil erosion and hillslope connectivity in the monsoonal tropics of northern Australia. In: *Earth Surf. Process. Landforms* 46 (10), S. 2110–2123. DOI: 10.1002/esp.5147.
Hänsel, Phoebe; Schindewolf, Marcus; Eltner, Anette; Kaiser, Andreas; Schmidt, Jürgen (2016): Feasibility of High-Resolution Soil Erosion Measurements by Means of Rainfall Simulations and SfM Photogrammetry. In: *Hydrology* 3 (4), S. 38. DOI: 10.3390/hydrology3040038.
Hazelhoff, L.; van Hoof, P.; Imeson, A. C.; Kwaad, F. J. P. M. (1981): The exposure of forest soil to erosion by earthworms. In: *Earth Surf. Process. Landforms* 6 (3-4), S. 235–250. DOI: 10.1002/esp.3290060305.
Herbst, M.; Bennett, N. C. (2006): Burrow architecture and burrowing dynamics of the endangered Namaqua dune mole rat (Bathyergus janetta) (Rodentia: Bathyergidae). In: *Journal of Zoology* 270 (3), S. 420–428. DOI: 10.1111/j.1469-7998.2006.00151.x.
Horn, B.K.P. (1981): Hill shading and the reflectance map. In: *Proc. IEEE* 69 (1), S. 14–47. DOI: 10.1109/PROC.1981.11918.
Imeson, A. C. (1977): Splash erosion, animal activity and sediment supply in a small forested Luxembourg catchment. In: *Earth Surf. Process. Landforms* 2 (2-3), S. 153–160. DOI: 10.1002/esp.3290020207.
Imeson, A. C.; Kwaad, F. J. P. M. (1976): Some Effects of Burrowing Animals on Slope Processes in the Luxembourg Ardennes. In: *Geografiska Annaler: Series A, Physical Geography* 58 (4), S. 317–328. DOI: 10.1080/04353676.1976.11879941.
Iserloh, T.; Ries, J. B.; Arnáez, J.; Boix-Fayos, C.; Butzen, V.; Cerdà, A. et al. (2013): European small portable rainfall simulators: A comparison of rainfall characteristics. In: *CATENA* 110 (2), S. 100–112. DOI: 10.1016/j.catena.2013.05.013.
James, M. R.; Robson, S. (2014): Sequential digital elevation models of active lava flows from ground-based stereo time-lapse imagery. In: *ISPRS Journal of Photogrammetry and Remote Sensing* 97 (3), S. 160–170. DOI: 10.1016/j.isprsjprs.2014.08.011.
Jones, Clive G.; Gutiérrez, Jorge L.; Byers, James E.; Crooks, Jeffrey A.; Lambrinos, John G.; Talley, Theresa S. (2010): A framework for understanding physical ecosystem engineering by

organisms. In: *Oikos* 119 (12), S. 1862–1869. DOI: 10.1111/j.1600-0706.2010.18782.x.

Kaiser, Andreas; Neugirg, Fabian; Rock, Gilles; Müller, Christoph; Haas, Florian; Ries, Johannes; Schmidt, Jürgen (2014): Small-Scale Surface Reconstruction and Volume Calculation of Soil Erosion in Complex Moroccan Gully Morphology Using Structure from Motion. In: *Remote Sensing* 6 (8), S. 7050–7080. DOI: 10.3390/rs6087050.

Kinlaw, A.; Grasmueck, M. (2012): Evidence for and geomorphologic consequences of a reptilian ecosystem engineer: The burrowing cascade initiated by the Gopher Tortoise. In: *Geomorphology* 157-158 (4), S. 108–121. DOI: 10.1016/j.geomorph.2011.06.030.

Kromer, Ryan; Walton, Gabe; Gray, Brian; Lato, Matt; Group, Robert (2019): Development and Optimization of an Automated Fixed-Location Time Lapse Photogrammetric Rock Slope Monitoring System. In: *Remote Sensing* 11 (16), S. 1890. DOI: 10.3390/rs11161890.

Kukko, Antero; Hyyppä, Juha (2009): Small-footprint Laser Scanning Simulator for System Validation, Error Assessment, and Algorithm Development. In: *photogramm eng remote sensing* 75 (10), S. 1177–1189. DOI: 10.14358/PERS.75.10.1177.

Larsen, A.; Nardin, W.; Lageweg, W. I.; Bätz, N. (2021): Biogeomorphology, quo vadis? On processes, time, and space in biogeomorphology. In: *Earth Surf. Process. Landforms* 46 (1), S. 12–23. DOI: 10.1002/esp.5016.

Le Hir, P.; Monbet, Y.; Orvain, F. (2007): Sediment erodability in sediment transport modelling: Can we account for biota effects? In: *Continental Shelf Research* 27 (8), S. 1116–1142. DOI: 10.1016/j.csr.2005.11.016.

Lehnert, Lukas W.; Thies, Boris; Trachte, Katja; Achilles, Sebastian; Osses, Pablo; Baumann, Karen et al. (2018): A Case Study on Fog/Low Stratus Occurrence at Las Lomitas, Atacama Desert (Chile) as a Water Source for Biological Soil Crusts. In: *Aerosol Air Qual. Res.* 18 (1), S. 254–269. DOI: 10.4209/aaqr.2017.01.0021.

Li, Guorong; Li, Xilai; Li, Jinfang; Chen, Wenting; Zhu, Haili; Zhao, Jianyun; Hu, Xiasong (2019a): Influences of Plateau Zokor Burrowing on Soil Erosion and Nutrient Loss in Alpine Meadows in the Yellow River Source Zone of West China. In: *Water* 11 (11), S. 2258. DOI: 10.3390/w11112258.

Li, Larry (2014): Time-of-Flight Camera – An Introduction. Technical White Paper. Hg. v. Texas Instruments. Online verfügbar unter https://www.ti.com/lit/wp/sloa190b/sloa190b.pdf, zuletzt geprüft am 22.12.2021.

Li, T. C.; Shao, M. A.; Jia, Y. H.; Jia, X. X.; Huang, L. M.; Gan, M. (2019b): Small‐scale observation on the effects of burrowing activities of ants on soil hydraulic processes. In: *Eur J Soil Sci* 70 (2), S. 236–244. DOI: 10.1111/ejss.12748.

Li, Tongchuan; Jia, Yuhua; Shao, Ming'an; Shen, Nan (2019c): Camponotus japonicus burrowing activities exacerbate soil erosion on bare slopes. In: *Geoderma* 348 (4), S. 158–167. DOI: 10.1016/j.geoderma.2019.04.035.

Li, Tongchuan; Shao, Ming’an; Jia, Yuhua; Jia, Xiaoxu; Huang, Laiming (2018): Small-scale observation on the effects of the burrowing activities of mole crickets on soil erosion and hydrologic processes. In: *Agriculture, Ecosystems & Environment* 261 (4), S. 136–143. DOI: 10.1016/j.agee.2018.04.010.

Longoni, Laura; Papini, Monica; Brambilla, Davide; Barazzetti, Luigi; Roncoroni, Fabio; Scaioni, Marco; Ivanov, Vladislav (2016): Monitoring Riverbank Erosion in Mountain Catchments Using Terrestrial Laser Scanning. In: *Remote Sensing* 8 (3), S. 241. DOI: 10.3390/rs8030241.

Malizia, Ana I. (1998): Population dynamics of the fossorial rodent Ctenomys talarum (Rodentia: Octodontidae). In: *Journal of Zoology* 244 (4), S. 545–551. DOI: 10.1111/j.1469-7998.1998.tb00059.x.

MALLALIEU, JOSEPH; CARRIVICK, JONATHAN L.; QUINCEY, DUNCAN J.; SMITH, MARK W.; JAMES, WILLIAM H.M. (2017): An integrated Structure-from-Motion and time-lapse technique for quantifying ice-margin dynamics. In: *J. Glaciol.* 63 (242), S. 937–949. DOI: 10.1017/jog.2017.48.

Meysman, Filip J. R.; Boudreau, Bernard P.; Middelburg, Jack J. (2003): Relations between local, nonlocal, discrete and continuous models of bioturbation. In: *Journal of Marine Research* 61 (3), S. 391–410. DOI: 10.1357/002224003322201241.

Monteverde, Martín J.; Piudo, Luciana (2011): Activity Patterns of the Culpeo Fox (Lycalopex Culpaeus Magellanica) in a Non-Hunting Area of Northwestern Patagonia, Argentina. In: *Mammal Study* 36 (3), S. 119–125. DOI: 10.3106/041.036.0301.

Morris, Rowena H.; Buckman, Solomon; Connelly, Paul; Dragovich, Deirdre; Ostendorf, Bertram; and Bradstock, Ross A. (2011): The dirt on assessing post-fire erosion in the Mount Lofty Ranges: comparing methods.

Nasermoaddeli, M. B.; Pasche, E. (2008): Application of terrestrial 3D scanner in quantification of the riverbank erosion and deposition. Institute of river and coastal engineering, Technical university Hamburg-Harburg, Hamburg,. Online verfügbar unter https://www.tuhh.de/t3resources/wb/Publikationen/MA-Veroeffentlichungen/nasermoaddelli/riverflow2008.pdf, zuletzt geprüft am 22.12.2021.

Pang, Xiao Pan; Guo, Zheng Gang (2017): Plateau pika disturbances alter plant productivity and soil nutrients in alpine meadows of the Qinghai-Tibetan Plateau, China. In: *Rangel. J.* 39 (2), S. 133. DOI: 10.1071/RJ16093.

Reichman, O. J.; Seabloom, Eric W. (2002): The role of pocket gophers as subterranean ecosystem engineers. In: *Trends in Ecology & Evolution* 17 (1), S. 44–49. DOI: 10.1016/S0169-5347(01)02329-1.

Richards, Paul J.; Humphreys, Geoff S. (2010): Burial and turbulent transport by bioturbation: a 27-year experiment in southeast Australia. In: *Earth Surf. Process. Landforms* 21 (2), n/a-n/a. DOI: 10.1002/esp.2007.

Ridd, Peter V. (1996): Flow Through Animal Burrows in Mangrove Creeks. In: *Estuarine, Coastal and Shelf Science* 43 (5), S. 617–625. DOI: 10.1006/ecss.1996.0091.

Romañach, Stephanie S.; Reichman, O. J.; Seabloom, E. W. (2005): Seasonal influences on burrowing activity of a subterranean rodent, Thomomys bottae. In: *Journal of Zoology* 266 (3), S. 319–325. DOI: 10.1017/S0952836905006941.

Rutin, J. (1996): The burrowing activity of scorpions (Scorpio maurus palmatus) and their potential contribution to the erosion of Hamra soils in Karkur, central Israel. In: *Geomorphology* 15 (2), S. 159–168. DOI: 10.1016/0169-555X(95)00120-T.

Sarbolandi, Hamed; Plack, Markus; Kolb, Andreas (2018): Pulse Based Time-of-Flight Range Sensing. In: *Sensors (Basel, Switzerland)* 18 (6). DOI: 10.3390/s18061679.

Schiffers, Katja; Teal, Lorna Rachel; Travis, Justin Mark John; Solan, Martin (2011): An open source simulation model for soil and sediment bioturbation. In: *PloS one* 6 (12), e28028. DOI: 10.1371/journal.pone.0028028.

Sharon, David (1980): The distribution of hydrologically effective rainfall incident on sloping ground. In: *Journal of Hydrology* 46 (1-2), S. 165–188. DOI: 10.1016/0022-1694(80)90041-4.

Thomsen, L. M.; Baartman, J. E. M.; Barneveld, R. J.; Starkloff, T.; Stolte, J. (2015): Soil surface roughness: comparing old and new measuring methods and application in a soil erosion model. In: *SOIL* 1 (1), S. 399–410. DOI: 10.5194/soil-1-399-2015.

Übernickel, Kirstin; Ehlers, Todd A.; Paulino, Leandro; Fuentes Espoz, Juan-Pablo (2021a): Time series of meteorological stations on an elevational gradient in National Park La Campana, Chile. Unter Mitarbeit von Kirstin Übernickel, Todd A. Ehlers, Leandro Paulino, Juan-Pablo Fuentes Espoz, Ramiro Bernales-Noguera, Willi Kappler et al.

Übernickel, Kirstin; Pizarro-Araya, Jaime; Bhagavathula, Susila; Paulino, Leandro; Ehlers, Todd A. (2021b): Reviews and syntheses: Composition and characteristics of burrowing animals along a climate and ecological gradient, Chile. In: *Biogeosciences* 18 (20), S. 5573–5594. DOI: 10.5194/bg-18-5573-2021.

Voiculescu, Mircea; Ianăş, Ana-Neli; Germain, Daniel (2019): Exploring the impact of snow vole (Chionomys nivalis) burrowing activity in the Făgăraș Mountains, Southern Carpathians (Romania): Geomorphic characteristics and sediment budget. In: *CATENA* 181 (1), S. 104070. DOI: 10.1016/j.catena.2019.05.016.

Wei, Xinghu; Li, Sen; Yang, Ping; Cheng, Huaishun (2007): Soil erosion and vegetation succession in alpine Kobresia steppe meadow caused by plateau pika—A case study of Nagqu County, Tibet. In: *Chin. Geograph.Sc.* 17 (1), S. 75–81. DOI: 10.1007/s11769-007-0075-0.

Wilkinson, Marshall T.; Richards, Paul J.; Humphreys, Geoff S. (2009): Breaking ground: Pedological, geological, and ecological implications of soil bioturbation. In: *Earth-Science Reviews* 97 (1-4), S. 257–272. DOI: 10.1016/j.earscirev.2009.09.005.

Yair, A. (1995): Short and long term effects of bioturbation on soil erosion, water resources and soil development in an arid environment. In: *Geomorphology* 13 (1-4), S. 87–99. DOI: 10.1016/0169-555X(95)00025-Z.

Yoo, Kyungsoo; Amundson, Ronald; Heimsath, Arjun M.; Dietrich, William E. (2005): Process-based model linking pocket gopher (Thomomys bottae) activity to sediment transport and soil thickness. In: *Earth Surf. Process. Landforms* 33 (11), S. 917. DOI: 10.1130/G21831.1.